



# *Sphagnum* and herbaceous net ecosystem exchanges in a Pyrenean peatland: a long-term study using the ISBA model

Raphael Garisoain<sup>1,2</sup>, Christine Delire<sup>1</sup>, Bertrand Decharme<sup>1</sup>, and Laure Gandois<sup>2</sup>

<sup>1</sup>Météo-France, CNRS, Univ. Toulouse, CNRM, Toulouse, France

<sup>2</sup>CRBE, Université de Toulouse, CNRS, Toulouse, France

**Correspondence:** Raphael Garisoain (raphael.garisoain@univ-tlse3.fr)

Received: 23 October 2025 – Discussion started: 27 November 2025

Revised: 23 April 2026 – Accepted: 24 April 2026 – Published: 20 May 2026

**Abstract.** Peatlands play a crucial role in the global carbon cycle, acting as long-term carbon sinks. However, their stability is increasingly threatened by climate change, particularly through rising temperatures and the intensification of droughts. This study focuses on the Bernadouze peatland in the Pyrenees Mountains and aims to validate a newly implemented *Sphagnum* Plant Functional Type (PFT) in the ISBA land surface model, assess the temporal evolution of carbon fluxes over the past 64 years, and investigate the factors influencing carbon accumulation, with a particular emphasis on drought events.

The model was validated using in situ data, demonstrating reasonable carbon flux estimations. Using this validated model, we reconstructed the net ecosystem exchange (NEE) dynamics of the Bernadouze peatland from 1959 to 2022. The results reveal significant interannual variability in NEE, largely driven by air temperature and water table depth. While the peatland has remained a carbon sink, extreme droughts such as those in 1989, 1994, 2003, and most recently 2022 have led to substantial CO<sub>2</sub> emissions.

Our findings suggest that although increasing temperatures have extended the growing season and enhanced gross primary productivity (GPP), the rising frequency and intensity of droughts pose a long-term risk to peatland carbon storage. The dryness index developed in this study appears to be a strong predictor of summer and annual NEE, offering a potential tool for estimating carbon fluxes in peatlands lacking direct measurements.

## 1 Introduction

Peatlands are vital to the global carbon cycle, serving as significant carbon reservoirs and actively exchanging CO<sub>2</sub> and methane with the atmosphere (Gorham et al., 2012). However, the stability of these carbon stocks is increasingly threatened by global warming (Page and Baird, 2016; Carter et al., 2012; Loisel et al., 2021), highlighting the need for precise models to predict their carbon balance. This concern is particularly relevant in mountainous regions, where climate change is expected to be more pronounced (Rogora et al., 2018), potentially affecting the functioning of mountain peatland ecosystems.

Models have been developed to represent the biophysical and biogeochemical processes that occur in peatlands. *Sphagnum* mosses are considered the dominant vegetation in Northern peatlands (Turetsky, 2003) and function differently from vascular plants, lacking stomata to regulate their water content (Clymo and Hayward, 1982). They acquire water either by absorbing atmospheric precipitation or through capillary action directly from the soil surface. Their presence is also crucial for the accumulation of organic carbon in peatlands, as they have a lower litter decomposition rate compared to vascular plants (Scheffer et al., 2001; Lang et al., 2009). As a result, various classes of models have been developed to account for the role of *Sphagnum* mosses, reflecting diverse approaches. Dynamic vegetation and ecosystem models, developed as offline tools without atmospheric, climate, or carbon feedbacks, have since incorporated these processes into their frameworks (Wania et al., 2009; Frolking et al., 2010; Walker et al., 2017; Gong et al., 2020; Metzger et al., 2016). Furthermore, specific Continental Surface

Models (CSMs) have been developed for the representation of peatlands (St-Hilaire et al., 2010; Wu and Blodau, 2013; Wu et al., 2016; Wania et al., 2013; Park et al., 2018). There have also been ongoing efforts to improve the representation of *Sphagnum* mosses in Global Land Surface models, with varying degrees of complexity and scope (Chadburn et al., 2015; Porada et al., 2016; Druel et al., 2017; Qiu et al., 2019; Shi et al., 2015; Grant et al., 2012; Shi et al., 2021).

Efforts to study peatland responses to drought episodes increasingly rely on field measurements and mesocosm experiments (Sterk et al., 2023; Robroek et al., 2024), though research in this area remains limited. A significant limitation of these methods is the scarcity of continuous field measurements capturing medium-term carbon fluxes over decades or longer. Such data would offer critical insights into the frequency and long-term effects of episodic drought events on carbon accumulation. Current carbon flux measurements are generally restricted to contemporary dynamics, which exhibit notable interannual variability, complicating efforts to extrapolate trends over medium or long-term timescales (Young et al., 2021). To explore long-term carbon accumulation dynamics, peat coring analyses provide a reliable means of determining the average Long-term apparent Rates of C Accumulation (LORCA), offering insights into millennia of accumulation (Turunen, 2003). Additionally, based on the same methodology, the Actual Rate of Carbon Accumulation (ARCA) can be determined, theoretically enabling the observation of carbon accumulation over decades or centuries (Chaudhary et al., 2017). Interest in ARCA has grown recently, particularly as a means of assessing the effects of climate and environmental changes on carbon accumulation. However, its reliability has been questioned (Young et al., 2021; Frolking et al., 2014), as ARCA does not accurately reflect the net balance of organic carbon in peatlands. An alternative approach involves modeling exercises that combine peat core age data with empirical models of organic matter decomposition. This allows reconstruction of historical carbon fluxes, linking absorbed and released carbon to initial peatland carbon stock (Yu, 2011; Packalen and Finkelstein, 2014; Frolking et al., 2010; Bunsen and Loisel, 2020; Loisel and Yu, 2013). In this study, we propose another complementary approach, leveraging a CSM that use atmospheric forcing data as input. Observationally-based atmospheric forcings, available with hourly resolution for some regions since the 1960s, provide a robust basis for modeling peatland evolution over the past several decades. Against the backdrop of Europe's severe drought in 2022 (Faranda et al., 2023), recent research on the Bernadouze peatland in the Pyrenees mountains identified a significant carbon release to the atmosphere during this event, supported by six years of field data (Garisoain et al., 2024). This drought presents a compelling case within a 64 year record, raising questions about its severity as an isolated event versus its representation of a broader trend. Additionally, it prompts examination of

whether the peatland's functioning during 2022 aligns with long-term behavior.

To address these questions, this study pursues three key objectives: (1) Implementation and first-site evaluation of a new *Sphagnum* Plant Functional Type (PFT) within the ISBA land surface model; (2) Assessment of the temporal evolution of carbon fluxes from the Bernadouze peatland over the past 64 years; (3) Investigation of the factors influencing carbon accumulation, with a particular focus on drought episodes.

## 2 Materials and methods

### 2.1 Study site

The Bernadouze peatland, located at an altitude of 1343 m in the eastern French Pyrenees (42.80273°N; 1.42361°E), covers roughly 4.7 ha and is part of a national biological reserve. Designated as a regional biological reserve since 1983 and a Natura 2000 site since 2007, it is one of the four sites of the French National Peatland Observatory Service SNO-Tourbieres. Characteristic of alpine and southwestern European mountainous peatlands, it is classified as a soligenous fen, continuously receiving water from precipitation and surface runoff. It has formed over the past 5000 years within a 1.4 km watershed with steep slopes averaging 50 %. A beech forest surrounds the fen, extending up to 1800 m. The peatland has an average peat depth of 2 m, reaching up to 6 m in some areas. The vegetation comprises species typical of both ombrotrophic areas, such as *Sphagnum palustre* and *Sphagnum capillifolium*, and minerotrophic areas, including *Carex demissa* and *Equisetum fluviatile* (Henry et al., 2014). This distribution is illustrated in Fig. 1 of Garisoain et al. (2023), which shows the spatial arrangement of vegetation types across the study site.

### 2.2 Environmental monitoring

Piezometer wells are 50 mm diameter PVC tubes, distributed across the peatland to cover the full spatial extent of the site (Fig. 1 from Garisoain et al., 2024), and their placement corresponds to the locations where chamber measurements were conducted. Water table depth (WTD) data were recorded at 1 h intervals, and the mean value from the nine piezometers is used throughout the study. As in precedent studies of the same peatland (Garisoain et al., 2023, 2024) we used the S2M reanalysis, which combines the French weather service SAFRAN meteorological reanalysis (8 km resolution) with the SURFEX/ISBA-Crocus snow cover model (Vernay et al., 2022). The S2M chain was applied in a local mode at the scale of the "Couserans" massif (a mountainous region in the central Pyrenees, southwestern France), assuming homogeneous weather conditions across the massif for equivalent altitudes but accounting for local topographic features in the calculation of shortwave radiation. The S2M model has a vertical resolution of 300 m and provides hourly out-

puts. The topographical features of the peatland, including altitude, slope, and aspect, were carefully accounted for to ensure that the atmospheric variables extracted for the site accurately represent local conditions.

### 2.3 Carbon fluxes

Hourly validated time series of CO<sub>2</sub> fluxes (GPP, ER, and NEE) spanning 2017 to 2022 are available, as detailed by Garisoain et al. (2024). These time series were derived from statistical models based on monthly CO<sub>2</sub> flux measurements using the static chamber technique. The use of the statistical model allows reconstruction of daily fluxes, enabling direct comparison with the ISBA model outputs at the same temporal resolution. The reconstructed fluxes are considered spatially representative of the peatland due to the coverage and replication of the chamber measurements. In the following sections, these reconstructed datasets are used as a reference for model validation, and readers should note that the validation is performed against the derived statistical model rather than the raw measurements.

### 2.4 Model development

In the present study, we utilize the ISBA model, which is part of the SURFEX land surface modeling platform (Version 9) and serves as the land surface component of the global Earth System Model CNRM-ESM (Delire et al., 2020). ISBA is widely employed to simulate surface processes, but it does not currently represent mosses or *Sphagnum*, which are essential components of ecosystems such as peatlands. To address this limitation, we introduce a new plant functional type (PFT) designed specifically for modeling mosses and *Sphagnum* within the ISBA framework. This work details the implementation of this novel PFT and the associated modifications to the model to better represent the dynamics of peatland ecosystems. The other PFTs, representing vegetation types such as herbaceous plants and trees, have been thoroughly described in the existing literature (Gibelin et al., 2008).

#### 2.4.1 Photosynthesis of *Sphagnum*

Plant photosynthesis is modeled according to the description by Goudriaan (1986) and Jacobs (1994), focusing on the equations involving the dependence on mesophyll conductance or CO<sub>2</sub> (Eq. 1) and light dependency (Eq. 2).

$$A_m = A_{m_{\max}} \times \left(1 - e^{-\frac{g_m^*(C_i - \Gamma)}{A_{m_{\max}}}}\right) \quad (1)$$

$A_m$  is the assimilation rate under light-saturated conditions ( $\text{kg m}^{-2} \text{s}^{-1}$ ),  $A_{m_{\max}}$  is the maximum assimilation rate ( $\text{kg m}^{-2} \text{s}^{-1}$ ),  $g_m^*$  is the mesophyll conductance without water stress ( $\text{m s}^{-1}$ ),  $C_i$  ( $\text{kg m}^{-3}$ ) is the internal mesophyll CO<sub>2</sub>

concentration (see Eq. 4) and  $\Gamma$  ( $\text{kg m}^{-3}$ ) is the CO<sub>2</sub> compensation point, meaning the CO<sub>2</sub> concentration below which the plant no longer fixes CO<sub>2</sub>.

$$A_n = (A_m + R_d) \times \left(1 - e^{-\frac{\epsilon I_a}{A_m + R_d}}\right) - R_d \quad (2)$$

$A_n$  is the net assimilation rate  $\text{kg m}^{-2} \text{s}^{-1}$ ,  $R_d$  is the “dark respiration”  $\text{kg m}^{-2} \text{s}^{-1}$ ,  $\epsilon$  the light use efficiency  $\text{kg J}^{-1}$  and  $I_a$  is the photosynthetically active radiation  $\text{W m}^{-2}$ .

$$R_d = \frac{A_m}{9} \quad (3)$$

$R_d$  is the mitochondrial respiration, empirically fixed.

In ISBA,  $g_m^*$  and  $A_{m_{\max}}$  depend on the PFT parameters and the leaf surface temperature following a  $Q_{10}$  function, modified by Collatz et al. (1992) to account for inhibitions (Jacobs et al., 1996). Then,  $g_m^*$  is replaced by  $g_m$ , which allows accounting for plant water stress conditions (see Table A1). Thus, the effect of stomatal closure on photosynthesis in ISBA is controlled by  $g_m$ , not by  $g_s$  (the stomatal conductance), which is calculated as a function of  $A_n$  and used solely to determine transpiration fluxes (see Eq. B5, Appendix B).

To model the photosynthesis of *Sphagnum* mosses, only mesophyll conductance has been considered to contribute to photosynthesis, even though the transfer of CO<sub>2</sub> within the hyaline cells is still poorly understood (Weston et al., 2015). Since *Sphagnum* mosses lack stomata, stomatal conductance is no longer defined for the *Sphagnum* PFT. Therefore, the relationship between *Sphagnum* moss photosynthesis and *Sphagnum* moss water content is accounted for through  $g_m$ . Shi et al. (2021) and Walker et al. (2017) described *Sphagnum* moss photosynthesis using the concept of total *Sphagnum* moss CO<sub>2</sub> conductance, derived from measurements by Williams and Flanagan (1998) relating *Sphagnum* moss water content to *Sphagnum* moss CO<sub>2</sub> conductance. In our case, we relate *Sphagnum* moss mesophyll conductance and total *Sphagnum* moss CO<sub>2</sub> conductance. Although they are not the same physical quantity. In Jacobs (1994) description,  $g_m$  is the closest approximation to total CO<sub>2</sub> conductance. Hence, the normalized total *Sphagnum* moss CO<sub>2</sub> conductance ( $g_{\text{tot}}$ ) was first defined following Gong et al. (2020) (Eq. 4 and Fig. A1). This variable was then used to parameterize the relationship between  $g_m$  and  $g_{\text{tot}}$  proposed by Williams and Flanagan (1998) (Eq. 5).

$$g_{\text{tot}} = \begin{cases} (\beta + \gamma \times w_{\text{Sp}} + \eta \times w_{\text{Sp}}^2) & \text{if } w_{\text{opt}} \geq w_{\text{Sp}} \geq w_{\text{min}} \\ (1 - 0.8 \times \frac{w_{\text{Sp}} - w_{\text{opt}}}{w_{\text{max}} - w_{\text{opt}}}) & \text{if } w_{\text{Sp}} \geq w_{\text{opt}} \\ 0 & \text{if } w_{\text{Sp}} \leq w_{\text{min}} \end{cases} \quad (4)$$

$$g_m = \alpha \times g_{\text{tot}} \quad (5)$$

$$\eta = \frac{\beta - 1}{w_{\text{opt}}^2} \quad (6)$$

$$\gamma = -2 \times w_{\text{opt}} \times \eta \quad (7)$$

Where  $w_{\text{Sp}}$  is the water content of *Sphagnum* mosses ( $\text{g g}^{-1}$ ),  $g_{\text{tot}}$  is the normalized total conductance,  $\beta$ ,  $\gamma$ ,  $\eta$  are coef-

ficients given in Table A2,  $w_{\min}$  and  $w_{\max}$  respectively the maximum and minimum water content of *Sphagnum* mosses ( $\text{g g}^{-1}$ ),  $w_{\text{opt}}$  ( $\text{g g}^{-1}$ ) is the water content of *Sphagnum* that maximizes  $g_{\text{tot}}$  and  $\alpha$  ( $\text{ms}^{-1}$ ) is a parametrized coefficient given in Table A2.

#### 2.4.2 Leaf area index – Canopy scaling

The evolution of *Sphagnum* moss biomass results from the balance between carbon assimilation through photosynthesis and *Sphagnum* moss mortality, calculated according to Eq. (8):

$$\frac{\Delta B}{\Delta t} = A_c - R_c - \frac{B}{\Delta t} \exp\left(\frac{-t}{\tau}\right) \quad (8)$$

where  $B$  is the active biomass of *Sphagnum* mosses in  $\text{kg m}^{-2}$ ,  $\frac{B}{\Delta t} \exp\left(\frac{-t}{\tau}\right)$  is the mortality of the *Sphagnum* moss biomass,  $\tau$  is the characteristic mortality time,  $\Delta t$  is a timestep of 1 d,  $A_c$  is the net assimilation of the *Sphagnum* mosses canopy and  $R_c$  is the respiration of *Sphagnum* mosses canopy ( $A_c = \text{LAI} \times A_n$ ,  $R_c = \text{LAI} \times R_d$ ).

The LAI is directly calculated from the leaf biomass reservoir  $B$  according to:

$$\text{LAI} = B \times \text{SLA} \quad (9)$$

where SLA (specific leaf area) is a foliar vegetation index representing the leaf area per unit of assimilated carbon ( $\text{m}^2 \text{m}^{-2} \text{kg}^{-1}$ ).

$$\text{SLA} = e \times N_m + f \quad (10)$$

Here,  $N_m$  is the mass-based nitrogen concentration in the leaf (Calvet and Soussana, 2001). The SLA is defined for each vegetation type.

Once net assimilation is calculated, multiplying by the LAI allows for scaling from the individual *Sphagnum* strand to the *Sphagnum* canopy. The ISBA model follows the assumption of maintaining constant temperature, humidity, and  $\text{CO}_2$  concentration throughout the canopy. Additionally, a radiative transfer model for photosynthetically active radiation was developed by Carrer et al. (2013), allowing for the representation of light diffusion within a canopy based on its LAI. This module accounts for the decrease in light radiation along the vertical profile of the canopy (with more light at the top of the canopy) as well as the diffusion of light towards the lower parts of the canopy. The attenuation of light within the canopy thus leads to a decreasing vertical profile of photosynthesis within the canopy. Leaf respiration, on the other hand, is assumed to be constant along the vertical profile of the canopy. Canopy respiration corresponds to the respiration calculated at the leaf level multiplied by the LAI.

#### 2.4.3 Biomass pools

In the original ISBA model, vegetation is represented by up to six biomass reservoirs: leaves, stem, wood, fine and coarse

roots, and a small storage pool corresponding to nonstructural carbohydrates (Gibelin et al., 2008; Delire et al., 2020). For grass/herbaceous PFTs, wood and coarse roots are excluded. Leaf biomass evolves based on photosynthetic carbon assimilation and is reduced by turnover, respiration, and allocation to other pools. Leaf area index (LAI) is derived from leaf biomass and specific leaf area, which depends on both PFT and nitrogen content. Mortality and turnover are PFT-dependent and climate-sensitive, especially for leaves. Photosynthesis and respiration are computed at sub-daily time steps, while the biomass pools evolve on a daily basis.

For *Sphagnum*, the structure was simplified to reflect its particular growth strategy and morphology. Only two biomass reservoirs are considered:  $B$ , representing the photosynthetically active green biomass, and  $B_{\text{brown}}$ , the dead biomass. The latter is fed by senescence from the green biomass and follows a similar formulation to the original model's decay processes, with an adjusted decay rate specific to *Sphagnum*. This minimalist representation captures the essential dynamics of *Sphagnum* growth and decomposition, consistent with its role in peat accumulation and its lack of differentiated organs like leaves or roots.

The brown *Sphagnum* mosses ( $B_{\text{brown}}$ ) are uniformly distributed over 10 cm of the soil profile, and this vertical distribution is maintained throughout the simulation.

#### 2.4.4 Sphagnum water content

To model the evolution of the water content in *Sphagnum* mosses, we followed the work of St-Hilaire et al. (2010), considering a linear relationship between the soil water content at 10 cm and the water content of *Sphagnum* mosses.

$$w_{\text{Sp}} = b \times w_{\text{soil}, 10 \text{ cm}} + c \quad (11)$$

where  $w_{\text{Sp}}$  is the water content of *Sphagnum* mosses in  $\text{g g}^{-1}$  and  $w_{\text{soil}, 10 \text{ cm}}$  is the soil water content at 10 cm in  $\text{m}^3 \text{m}^{-3}$ . The empirical coefficients  $b$  and  $c$  are given in Table A2.

The precipitation interception reservoir is considered negligible. Consequently, *Sphagnum* mosses receive water primarily through capillary action from the soil within 10 cm of the surface. Although direct interception of rainfall also contributes in reality, this process is not explicitly modeled here. Instead, we account only for the effect of capillarity by relating the water content of *Sphagnum* to that of the upper 10 cm of soil. Precipitation that would otherwise be intercepted bypasses the moss canopy and infiltrates directly into the soil, thereby influencing both soil and *Sphagnum* water content.

#### 2.4.5 Sphagnum evaporation

Given that *Sphagnum* mosses do not possess stomata, we consider that the latent heat flux from the vegetation is solely due to the evaporation of water from their epidermal cells. The plant transpiration phenomenon controlled by stomata is therefore eliminated here. Thus, we have:

$$E_{veg} = \frac{F_{veg}}{R_a + R_{sp}} \times (q_{sat}(T_s) - q_a) \times \rho_a$$

$$\text{with } R_a = \frac{1}{C_H V_a} \quad (12)$$

$E_{veg}$  is the latent heat flux from the vegetation (see Eq. B5, Appendix B) in  $\text{kg m}^{-2} \text{s}^{-1}$ .  $R_a$  and  $R_{sp}$  represent the air and *Sphagnum* canopy resistances, respectively.  $F_{veg}$  is the fraction of vegetation,  $q_{sat}(T_s)$  is the specific humidity at saturation at temperature  $T_s$ ,  $T_s$  is the surface temperature and  $q_a$  is the specific humidity of the air at reference altitude  $z_a$ .  $\rho_a$  is the air density at altitude  $z_a$ ,  $C_H$  is the drag coefficient, and  $V_a$  is the wind speed at  $z_a$ .

$R_{sp}$  has been modeled following the work of Bond-Lamberty et al. (2011) and Gong et al. (2020), who experimentally established a relationship between the resistance of the *Sphagnum* canopy and the water content of the *Sphagnum* mosses. The *Sphagnum* moss resistance to water decreases towards low values when the water content of the *Sphagnum* mosses is high, leading to strong evaporation. Below a threshold value, as the *Sphagnum* mosses dry out, the resistance of the *Sphagnum* mosses increases linearly, allowing to retain a minimal threshold of water in the *Sphagnum* mosses. As such, we define:

$$R_{sp} = \max\left(\frac{1}{\text{SWI}_{sp}/d}, R_{sp,\min}\right) \quad (13)$$

with  $d$  in  $\text{sm}^{-1}$ ,  $d$  and  $R_{sp,\min}$  given in Table A2.

By choosing this approach, we diverge significantly from Bond-Lamberty et al. (2011) and Gong et al. (2020), who link bulk resistivity to the water content of *Sphagnum* mosses. Here, we disregard the water content of *Sphagnum* mosses and instead directly use the soil water content at 10 cm depth through the *Sphagnum* Soil Wetness Index ( $\text{SWI}_{sp}$ ). However, this new formulation remains consistent with previous ones when representing the *Sphagnum* canopy resistance ( $R_s$ ) as a function of the water content of *Sphagnum* mosses (Fig. A2).

Following Decharme et al. (2016) to account for soil water stress by using the Soil Wetness Index we define the *Sphagnum* Soil Wetness Index:

$$\text{SWI}_{sp} = \sum_j \text{sphafrac}_j \max\left(10^{-4}, \min\left(\frac{w_{\text{soil},j} - w_{\text{wilt},j}}{w_{\text{fc},j} - w_{\text{wilt},j}}, 1\right)\right) \quad (14)$$

Here,  $\text{sphafrac}_j$  is the proportion of brown *Sphagnum* in layer  $j$ ,  $w_{\text{soil},j}$  is the soil water content of layer  $j$ ,  $w_{\text{fc},j}$  is the soil water content at field capacity of layer  $j$ , and  $w_{\text{wilt},j}$  is the soil water content at wilting point of layer  $j$ , all in  $\text{m}^3 \text{m}^{-3}$ .

$\text{SWI}_{sp}$  varies between  $10^{-4}$  when the soil water content of the *Sphagnum* zone is less than or equal to the wilting point, and 1 when water is not a limiting factor. Beyond 10 cm depth where we assume there are no living *Sphagnum* anymore,  $\text{SWI}_{sp} = 0$ .

The resistance of *Sphagnum* mosses to water is inversely proportional to the availability of water in the surface layers of the soil. The more water there is in the surface layers, the lower the resistance, with a minimum value of  $R_s = 1$ . The resistance then increases according to the inverse function as the water content of the soil decreases. The water evaporated by the *Sphagnum* mosses is then removed from the top 10 cm of soil, proportional to the layer depth from each layer concerned.

#### 2.4.6 Soil physics

The ISBA model resolves soil heat and water exchanges using a 14-layer scheme over 12 m depth, minimizing numerical errors in diffusion equations. Thermal depth remains constant at 12 m, while hydrological depth varies with vegetation. The surface energy balance combines properties of snowpack and soil/vegetation. A 12-layer snow model by Boone and Etchevers (2001) and improved by Decharme et al. (2016) simulates snow properties like energy absorption, density, and melt processes, considering surface albedo and radiation absorption. Heat transfer in soil follows Fourier’s law, accounting for soil water content, porosity, and conductivity. Water mass fluxes are described using the Richards equation, incorporating precipitation, snowmelt, freezing/thawing, and vapor transport. Soil hydraulic properties relate to water content and soil texture, with adjustments for ice presence.

#### 2.4.7 Carbon pools in soil

The ISBA model balances plant debris decomposition and microbial activity to represent soil carbon stocks, based on the CENTURY model (Parton et al., 1993). Plant debris, including leaves, stems, and roots, is divided into structural and metabolic litter reservoirs, above and belowground. These decompose into three types of soil carbon reservoirs: fast (less than a year), slow (about a decade), and passive (hundreds to thousands of years). This decomposition process drives soil heterotrophic respiration, releasing  $\text{CO}_2$  (Gibelin et al., 2008).

#### 2.4.8 Thermal and hydraulic properties of peat soils

ISBA calculates thermal and hydraulic properties of soil by combining mineral soil attributes with those of soil organic carbon (SOC), adjusted for the organic matter proportion in each layer. We keep the same method for peat soils. Peat organic matter density is defined using porosity and the density of pure organic matter ( $1300 \text{ kg m}^{-3}$ ). In our simulations, the SOC fraction in each layer is fixed at 1, reflecting the assumption of a completely organic soil. Peat porosity ranges from 0.930 in surface fibric soil to 0.845 in deeper sapric soil, significantly affecting both the thermal conductivity and water retention capabilities of the soil. These variations influence organic matter density and overall soil properties,

particularly in peat soils, ensuring accurate modeling of soil thermal and hydraulic dynamics (Decharme et al., 2016).

### 2.4.9 Biogeochemical processes in peat

The research conducted by Morel et al. (2019) has led to the development of a biogeochemical module capturing various physical and chemical processes occurring within peatlands. This module discretizes the soil into 14 layers, with soil physics resolved for each. It calculates the concentrations of O<sub>2</sub>, CO<sub>2</sub>, and CH<sub>4</sub> in each layer, enabling representation of biogeochemical processes across the entire vertical profile. Hence, processes such as methanogenesis in anaerobic conditions, methanotrophy (methane oxidation to CO<sub>2</sub> in the presence of O<sub>2</sub>), and heterotrophic respiration (production of CO<sub>2</sub>), are described within ISBA. Soil water level and thus O<sub>2</sub> concentration in peat regulate these chemical processes. Various equations account for the three different gas transport mechanisms in peat, including transport by plants, ebullition, and diffusion.

The carbon accumulation in the soil and its transfer between layers are represented by an advection term considered constant at 2 mm yr<sup>-1</sup> (Guenet et al., 2013). The phenomenon of cryoturbation, i.e., the mixing of surface peat layers due to freezing and thawing, is modeled using a diffusion equation following Koven et al. (2009).

### 2.4.10 Ecosystem respiration

Ecosystem respiration is defined here as the combination of heterotrophic respiration across the peat profile and autotrophic respiration from surface vegetation.

Heterotrophic respiration is calculated for each of the 14 soil layers, based on the CO<sub>2</sub> concentration in each layer. Two sources of CO<sub>2</sub> are modeled for each layer: the production of CO<sub>2</sub> from organic matter decomposition (CO<sub>2,oxic</sub>) and the production of CO<sub>2</sub> resulting from methane oxidation (CO<sub>2,methane</sub>), indirectly linked to methane concentration in each layer and thus to methanogenesis.

$$\text{CO}_{2,\text{oxic}}^i(z) = \theta(z)k_i(z, \text{Tg})C_i(z) \times \min\left(1, \frac{C_{\text{max}}(z)}{\Delta t} \frac{1}{\sum_j \theta(z)k_j(z, \text{Tg})C_j(z)}\right) \quad (15)$$

Here,  $i$  and  $j$  represent the types of carbon reservoirs (metabolic and structural litter, active C, slow C, passive C). CO<sub>2,oxic</sub> production is determined by the organic matter decomposition rate ( $\theta(z)k_i(z, \text{Tg})$ ), which initially depends on soil temperature and moisture content (Morel et al., 2019). The function  $\theta(z)$ , varying between 0.05 (dry soil) and 1 (above field capacity), accounts for soil moisture impact on microbial activity. In this study, soil moisture did not appear to strongly constrain organic matter decomposition in near surface moss dominated layers as indicated by the closer agreement between ISBA and observed (statistically modelled) soil respiration when  $\theta(z)$  was excluded (Fig. A4b and

e). We nevertheless aimed to preserve contrasting drought responses across vegetation types. Therefore,  $\theta(z)$  was removed for *Sphagnum*, while it was retained for herbaceous to maintain drought sensitivity where moisture deficits are expected to constrain belowground carbon turnover. The decomposition rate ( $k_i(\text{Tg})$ ) follows an Arrhenius-like equation ( $Q_{10}$ ), accounting for increased decomposition with temperature rise. The last part of the equation considers oxygen availability with  $C_{\text{max}}(z)$  representing the maximum carbon mass producible from available oxygen.

Methane oxidation  $\text{CH}_4 + 2\text{O}_2 \rightarrow \text{CO}_2 + 2\text{H}_2\text{O}$  contributes to CO<sub>2</sub> production, especially in deeper layers. For litter above ground, CO<sub>2</sub> is directly released to the atmosphere. In deeper layers, diffusion, plant-mediated transport (PMT), and evapotranspiration facilitate CO<sub>2</sub> escape. Gas diffusion in soil layers leads to vertical gas movements based on concentration gradients. PMT depends on leaf area index (LAI), while evapotranspiration is influenced by PFT.

### 2.5 Water table depth diagnosis and dryness index development

First, based on the ISBA outputs, we derived Eq. (16), which relates, for each soil layer, the change in volumetric water content to the change in water equivalent height, assuming the layer is saturated.

$$w_{j,\text{sat}}(t) \frac{\partial h_j(t)}{\partial t} = d_j \frac{\partial w_{j,\text{soil}}(t)}{\partial t} \quad (16)$$

with  $w_{j,\text{sat}}$  the volumetric water content of soil layer  $j$  at saturation,  $h_j$  the height of water in the layer  $j$ ,  $d_j$  the vertical width of the layer  $j$ ,  $w_{j,\text{soil}}$  the volumetric water content of soil layer  $j$ .

Then, we derived the ISBA-diagnosed WTD by summing over the soil layers down to 2 m depth, i.e. those where variations in water content are significant. This calculation assumes that the variation of  $w_{\text{sat}}$  with depth  $z$  is negligible, allowing it to be factored out of the summation (see Fig. A3a):

$$\text{WTD}_{\text{ISBA}} = \sum_j \Delta h_j = \sum_j \frac{\Delta w_{j,\text{soil}} \times d_j}{w_{j,\text{sat}}} \quad (17)$$

where  $\Delta h_j$ , and  $\Delta w_{j,\text{soil}}$  represent the changes in water equivalent height and soil volumetric water content, respectively, calculated explicitly through the temporal discretization of Eq. (16).

The dryness index is based on the work of Garisoain et al. (2024) (see Fig. A3b). We first define the daily soil water deficit  $\text{dif}(t)$ :

$$\text{dif}(t) = T_{\text{air,normalized}}(t) - \text{WTD}_{\text{normalized}}(t) \quad (18)$$

We use the daily mean of  $T_{\text{air}}(t)$  and  $\text{WTD}(t)$  to calculate  $\text{dif}(t)$ . Normalization of each variable ( $X$ ) was done following  $X_{\text{normalized}} = \frac{X - X_{\text{min}}}{X_{\text{max}} - X_{\text{min}}}$ . A minimum WTD value of 1 m was imposed to elevate the normalized WTD values, since

the diagnosed WTD tends to produce water tables that do not drop sufficiently during droughts. This adjustment allows the normalized WTD to better discriminate drought periods, which would otherwise be overly smoothed by the index (see Fig. A3b).

To consider only periods of positive water deficit, we define the function  $f(t)$  as:

$$f(t) = \begin{cases} \text{dif}(t), & \text{if } \text{dif}(t) > 0 \\ 0, & \text{otherwise} \end{cases} \quad (19)$$

The Dryness Index (DI) is then calculated by integrating  $f(t)$  over the summer period:

$$\text{DI} = \int_{\text{july}}^{\text{august}} f(t) dt \quad (20)$$

This formulation ensures that only days with a positive soil water deficit contribute to the DI, providing a simple and physically meaningful measure of summer dryness.

## 2.6 Statistical analyses

To compute Pearson correlation coefficients ( $r^2$ ), root mean square errors (RMSE) trends and associated  $p$  values, we used the statsmodels Python library. In particular, the Ordinary Least Squares (OLS) ([https://www.statsmodels.org/dev/generated/statsmodels.regression.linear\\_model.OLS.html](https://www.statsmodels.org/dev/generated/statsmodels.regression.linear_model.OLS.html), last access: 11 May 2026) regression function was employed to fit a linear model and perform an  $F$ -test to assess the statistical significance of the relationship.

To assess the relative contribution of each season to interannual variability in net ecosystem exchange (NEE) (Fig. 6), we applied SHAP (SHapley Additive exPlanations), a game-theoretic approach widely used for interpreting machine learning models. Specifically, we trained an Ordinary least squares Linear Regression model from sklearn python library ([https://scikit-learn.org/stable/modules/generated/sklearn.linear\\_model.LinearRegression.html](https://scikit-learn.org/stable/modules/generated/sklearn.linear_model.LinearRegression.html), last access: 11 May 2026) to predict annual NEE from seasonal values (summer, autumn, spring, and winter). We then used SHAP values to estimate how much each seasonal predictor contributed to the model output. Rather than relying on model coefficients or explained variance, we computed the mean absolute SHAP values across all observations to quantify each season's average influence. These contributions were normalized to express their relative importance as percentages. This approach provides a robust and interpretable measure of feature relevance, even for collinear predictors. The SHAP methodology is described in detail at: <https://shap.readthedocs.io/en/latest/index.html> (last access: 11 May 2026).

A simple linear model using  $R^2$  or an  $F$ -test tends to attribute explanatory power to the first variables entered into the model. When predictors are correlated as is the case here

with seasonal NEE components (e.g., summer NEE, autumn NEE) this can lead to shared variance being unfairly credited to one variable over another. In contrast, SHAP values, based on Shapley values from cooperative game theory, average the contribution of each variable across all possible combinations of input features. This results in a fair and consistent allocation of importance, even when variables are highly interdependent or collinear.

## 2.7 Experimental protocol

At the Bernadouze site, we obtained a 64-year meteorological data series (1959–2022) from the S2M reanalysis, which was used as input for the ISBA land surface model. To establish a contemporary carbon balance for the various carbon compartments, we simulated a 7000-year spin-up to account for the peatland's age, repeating the 64 year atmospheric forcing. This approach ensured a realistic accumulation of carbon in the soil reservoirs. The model was run in a one-dimensional configuration, at a single grid point corresponding to the location of the Bernadouze peatland.

For model validation (Sect. 3), we contrast simulations with 100% *Sphagnum* cover and 100% herbaceous cover. Herbaceous cover was simulated with the use of the ISBA PFT boreal grassland (BOGD). For the remainder of the study (Sect. 4), the vegetation distribution is assumed to consist of 70% herbaceous plants and 30% *Sphagnum* mosses, based on the cartography provided by Henry et al. (2014). Accordingly, the GPP, ER, and NEE values presented correspond to this vegetation mix. A subsection is dedicated to analyzing the sensitivity of carbon fluxes to vegetation composition.

## 3 Model validation over the 2017–2023 period

### Carbon fluxes

Figure 1 compares three time series from 2017 to 2023, illustrating Gross Primary Productivity (GPP), Ecosystem Respiration (ER) and Net Ecosystem Exchange (NEE) modeled by a statistical model (grey) and the ISBA model for *Sphagnum* (orange) and Herbaceous (blue). The top plot (a) shows GPP with  $r^2$  values of 0.6 and 0.62 (RMSE of 1.9 and 1.6  $\mu\text{mol}^{-2} \text{s}^{-1}$ , see Fig. A4a, b), indicating moderate agreement between the models. The middle plot (b) shows ER with  $r^2$  values of 0.82 and 0.44 (RMSE of 0.9 and 1.6  $\mu\text{mol}^{-2} \text{s}^{-1}$ , Fig. A4d, e), revealing stronger agreement for ER, particularly for *Sphagnum* respiration. The bottom plot, Fig. A4c, f, shows NEE with  $r^2$  values of 0.1 and 0.2 (RMSE of 1.6 and 1.3  $\mu\text{mol}^{-2} \text{s}^{-1}$ ). Additional scatter plots for the mixed vegetation configuration (Fig. A4g–i) highlight contrasted performances across fluxes. For GPP, the mixed simulation shows a level of agreement comparable to that of herbaceous vegetation alone ( $r^2 = 0.62$ , RMSE = 1.58  $\mu\text{mol}^{-2} \text{s}^{-1}$ ). For ER, the mixed con-

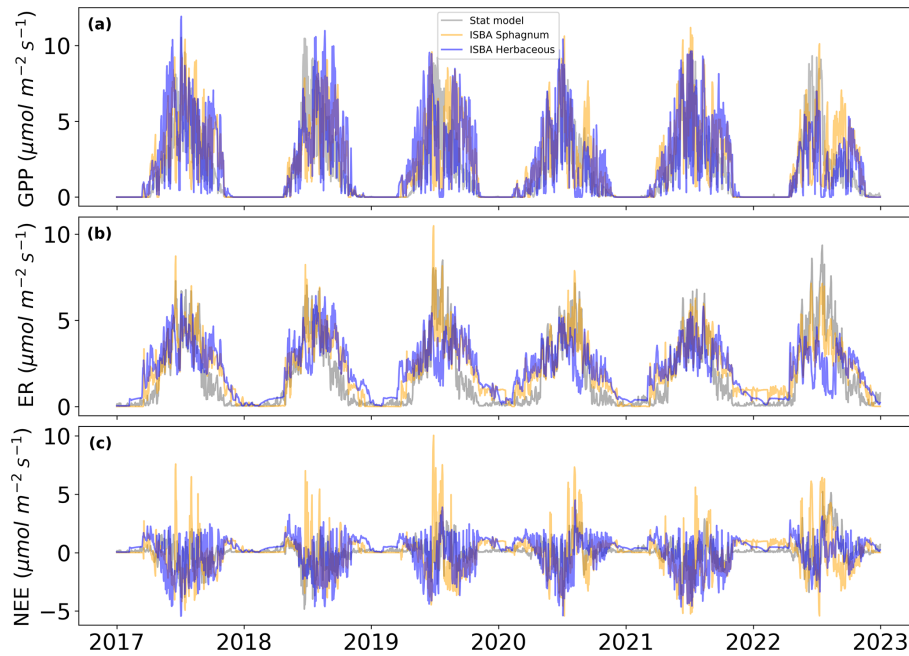


**Figure 1.** Daily (a) gross primary productivity and (b) ecosystem respiration fluxes compared between statistical models (grey) (Garisoain et al., 2024) and ISBA over the 2017–2022 period for herbaceous (blue) and *Sphagnum* mosses (orange).

figuration exhibits an intermediate performance, but with a substantial improvement compared to herbaceous vegetation alone ( $r^2 = 0.60$ ,  $\text{RMSE} = 1.32 \mu\text{mol}^{-2} \text{s}^{-1}$ ). For NEE, the mixed simulation yields higher skill scores ( $r^2 = 0.24$ ,  $\text{RMSE} = 1.17 \mu\text{mol}^{-2} \text{s}^{-1}$ ) than either vegetation type considered separately, although overall correlations remain low.

The ISBA model captures the interannual variability of GPP, ER and NEE effectively (Fig. A5), Consistently showing slightly higher values at the beginning of the growing season, much higher values at the end of the growing season, and stronger winter ecosystem respiration (ER) compared to the statistical model. Herbaceous vegetation is more sensitive to summer droughts than *Sphagnum*, leading to reduced GPP and ER in summer, especially during the 2022 drought, which caused a sharp decline in herbaceous GPP and ER.

### 3.0.1 Water table depth

Figure 2 compares the mean water table depth (WTD) from in situ measurements (grey with shaded standard deviation) to the ISBA diagnosed WTD (orange for *Sphagnum* mosses and blue for herbaceous) over the period 2017–2022. The ISBA model generally follows the observed data, capturing the overall trends and seasonal variations (Fig. A5) in WTD although there are occasional deviations, particularly at the end of the growing season and during drought events where the observed data shows higher variability. Overall, the ISBA model demonstrates rather satisfactory performance in simulating WTD ( $r^2 = 0.47$ ,  $\text{RMSE} = 0.09 \text{ m}$  for herbaceous,  $r^2 = 0.33$ ,  $\text{RMSE} = 0.1 \text{ m}$  for *Sphagnum*

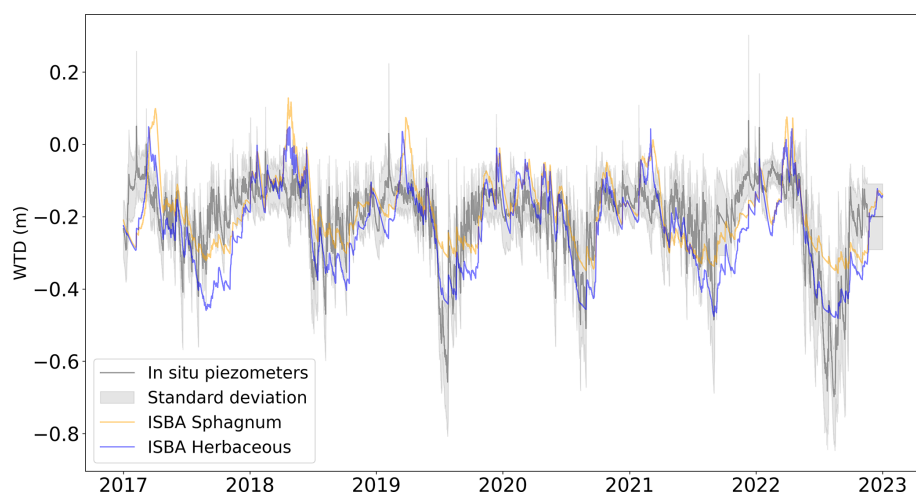
and  $r^2 = 0.45$ ,  $\text{RMSE} = 0.09 \text{ m}$  for the mixed vegetation, Fig. A6). The simulated WTD with herbaceous plants is consistently lower than with *Sphagnum* mosses.

## 4 Results: Water and carbon balance of the peatland over the last 60 years

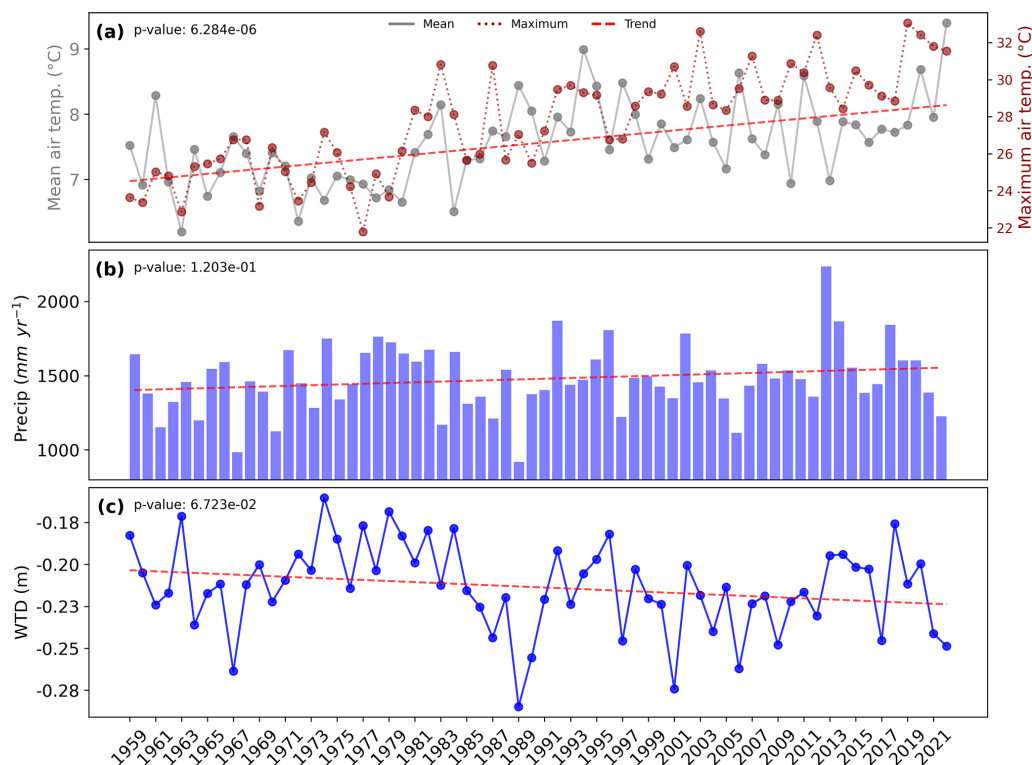
### 4.1 Environmental variables

Figure 3 consists of three panels, labeled (a), (b), and (c), illustrating the evolution of mean and maximum annual temperature, annual cumulative precipitation, and annual mean water table depth (diagnosed from ISBA) from 1959 to 2022, along with their respective trends and  $p$  values. Annual mean temperature (a) shows a significant ( $p$  value  $< 0.05$ ) increasing trend over the years. The annual mean temperature increases from approximately  $7^\circ\text{C}$  in the early years to about  $9^\circ\text{C}$  by 2022. Annual maximum temperature shows a similar evolution with an increase up to  $8^\circ\text{C}$  from 1959 to 2022.

Annual cumulative precipitation (b) ranges from approximately 1000 to 2250 mm, while the Water Table Depth (WTD) (c) varies between  $-0.16$  and  $-0.29 \text{ m}$  over the whole period. A steady increase in the level of the water table is observed from 1967 to 1983, followed by a sharp decline, reaching its minimum in 1989. After this, the WTD rises again and stabilizes, although notable interannual fluctuations persist until the end of the period. Interestingly, the fluctuations in annual precipitation closely mirror those of the mean annual WTD, suggesting a strong correlation be-



**Figure 2.** Hourly in situ mean water table depth is shown in grey, with its standard deviation in shaded areas, compared to the hourly diagnosed water table depth of ISBA over the 2017–2022 period for two different types of vegetation herbaceous (blue) and Sphagnum mosses (orange).



**Figure 3.** (a) Mean and maximum annual air temperature (°C) and (b) annual cumulative precipitation mm yr<sup>-1</sup> both from the S2M reanalysis and (c) mean water table depth (m) diagnosed from ISBA outputs, along with their trends as red dashed lines and corresponding  $p$  values.

tween these two variables. The trends of annual cumulative precipitation and annual mean WTD move in opposite directions, with precipitation increasing and the level of the water table decreasing. However, both trends are not significant ( $p$  values  $> 0.05$ ).

## 4.2 Net ecosystem exchanges

This section analyzes long term NEE dynamics and their drivers using ISBA simulations forced by the S2M reanalysis. Unless stated otherwise, all simulations and analyses presented in this section use the site vegetation distribution

derived from Henry et al. (2014), i.e., 70 % herbaceous plants and 30 % *Sphagnum* mosses.

#### 4.2.1 An overall carbon sink despite strong inter-annual variability

Figure 4 illustrates (a) the annual Net Ecosystem Exchange (NEE) and (b) the cumulative NEE from 1959 to 2022. The lowest annual NEE is modelled in 2011 ( $-171 \text{ g C m}^{-2} \text{ yr}^{-1}$ ), while the highest value occurs in 2022 ( $122 \text{ g C m}^{-2} \text{ yr}^{-1}$ ). Panel (b) shows a long-term decrease in cumulative NEE, indicating that the ecosystem acts as a net carbon sink over the entire study period. Piecewise linear trends computed for three successive 22 year periods (1959–1980, 1980–2001, and 2001–2022) reveal a progressive intensification of carbon uptake, as evidenced by increasingly negative slopes of cumulative NEE. The comparison of slopes between periods indicates that this intensification is not linear through time. The strongest increase in carbon sequestration occurs between the first and second periods, while the rate of intensification decreases after the early 2000s, suggesting a slowdown in the acceleration of the carbon sink despite continued strengthening.

Interannual variability, quantified by the standard deviation of annual NEE and reported as text annotations for each period, shows a marked temporal evolution. Variability is highest during the early period (1959–1980), decreases substantially during the phase of strongest sink intensification (1980–2001), and slightly increases again during the most recent period (2001–2022). This pattern suggests that the period of rapid carbon sink strengthening coincides with a more stable interannual behaviour, whereas recent decades combine sustained carbon uptake with a renewed increase in year-to-year variability.

Overall, despite substantial annual fluctuations, the long term signal remains robust and highlights a persistent accumulation of carbon by vegetation over the past six decades.

#### 4.2.2 Seasonality of GPP, ER and NEE over the 1959–2022 period

Figure 5 depicts the seasonal mean and interannual variability in gross primary production (a), ecosystem respiration (b), and net ecosystem exchange (c) over several time periods, specifically 1959–1980 (blue), 1980–2001 (orange), and 2001–2022 (green), with a focus on the year 2022 both from ISBA (red line) and the statistical model (purple line). Periods of approximately 22 years were chosen to ensure statistically robust trend estimates, following common climatological practice for analysing multi-decadal variability. Given the 64 year length of the record, three successive periods were defined with a slight overlap, allowing each period to be long enough for robust linear trends while maintaining three comparable intervals (World Meteorological Organization, 2017). Each subplot shows cumulative val-

ues with their respective mean and interannual variability at 90 % confidence interval. In panel (a), GPP values are negative, indicating carbon uptake by vegetation, with more pronounced uptake during the growing season (April to September). Panel (b) shows ER values, which are positive, representing carbon release. Respiration increases during warmer months, with higher rates, suggesting intensified ecosystem respiration. Panel (c) combines GPP and ER to show NEE. The GPP intensifies over time and becomes increasingly pronounced across the three periods. The same trend is observed for respiration. As a combination of these two variables, NEE exhibits greater seasonal variability, which is not necessarily easy to grasp from this graph but is more apparent in Fig. 6. The mean NEE values for the periods 1980–2001 and 2001–2022 show a similar trend, except during winter, when the NEE of the 2001–2022 period shifts towards positive values. Nonetheless, over the annual cycle, both of these periods display more negative NEE values compared to the 1959–1980 period.

The seasonality of GPP (a) and ER (b) has gradually intensified over time, as observed in the three periods. For NEE (c), the trend is less straightforward, but its seasonality has become increasingly pronounced. Additionally, the duration of the growing season has extended, as reflected by the earlier spring and later summer inflection points of cumulative NEE (solid blue, orange and green curves (panel c)).

Focusing on 2022, the NEE curve (red) deviates entirely from the interannual variability of the three periods combined, starting in July and continuing through November. Comparing this with the statistical model for 2022 (purple curve), we observe that despite differences in seasonality between ISBA and the statistical model, both agree in highlighting 2022 as a year significantly outside the confidence intervals. While GPP and ER for 2022 remain within the 2001–2022 interannual variability, the GPP is notably close to the lower limit ( $-$  GPP to the upper limit), underscoring the exceptional nature of this year in terms of carbon flux dynamics.

Figure 6a shows that across all time periods, summer is the season contributing the most to annual NEE variability, accounting for approximately 39 % of the total contribution over the 1959–2022 period. Autumn and spring follow, alternating in second place depending on the period, with comparable contributions of around 23 %–25 %. Winter consistently exhibits the lowest contribution, around 11 % of the annual NEE variability. The distribution of signed SHAP values for the full period (Fig. 6b) further highlights the seasonal dynamics. Summer displays a wide variability, with the median and central 50 % of values slightly below zero, but with long positive tails reflecting years with strong  $\text{CO}_2$  release to the atmosphere. Autumn is generally shifted toward positive values, with extreme positive contributions in some years. Spring is centered slightly below zero, with extremes toward negative values. Winter shows relatively low variability, with a skewed distribution including many neg-

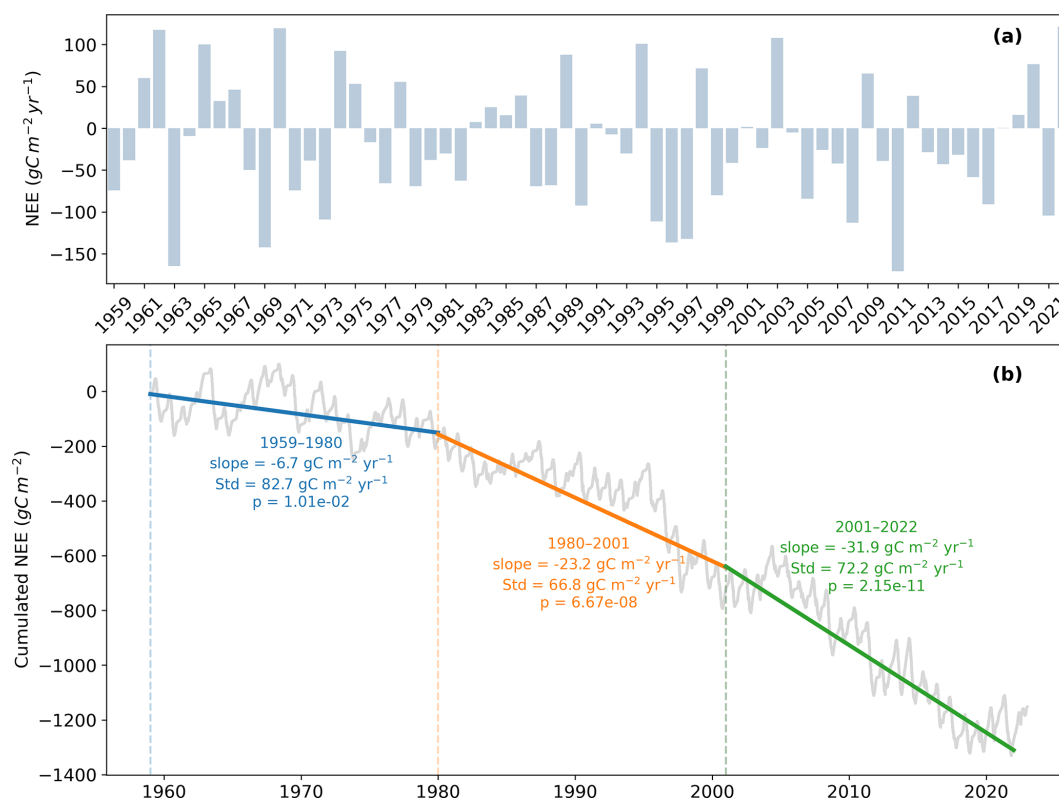


**Figure 4.** (a) Annual net ecosystem exchange ( $\text{gC m}^{-2} \text{yr}^{-1}$ ) from 1959 to 2022, as simulated by ISBA. (b) Hourly cumulated net ecosystem exchange ( $\text{gC m}^{-2}$ ) from 1959 to 2022, also from ISBA. The panel additionally reports the linear trend (slope), its  $p$  value, and the standard deviation of annual NEE for three distinct periods: 1959–1980, 1980–2001, and 2001–2022.

ative contributions but a long positive tail, indicating occasional meaningful contributions despite its overall smaller role. Overall, these results confirm that summer dominates the interannual variability of annual NEE, but also reveal that other seasons particularly autumn and spring can contribute substantially in certain years. This supports the focus on summer NEE drivers while recognizing the importance of seasonal context.

#### 4.3 Joint Influence of Air Temperature and Water Table Depth on Summer NEE Variability

Panel (a) of Fig. 7 shows the evolution of cumulative summer NEE (red) compared to cumulative annual NEE (blue) from 1959 to 2022. The cumulative summer NEE tends to “drive” the cumulative annual NEE almost always sharing the same sign, except in years near equilibrium (cumulative annual NEE = 0). This relationship is supported by a strong correlation between summer and annual cumulative NEE ( $r^2 = 0.71$ , Fig. A7) and by the fact that summer NEE contributes approximately 40 % of the interannual variability of cumulative NEE (Fig. 6).

Panel (b) illustrates the evolution of the dryness index from 1959 to 2022. The trend shows an increasing pattern, with  $p = 0.054$ , which is slightly above the conventional sig-

nificance threshold of 0.05. As the dryness index increases, the cumulative summer NEE also increases, showing a good correlation ( $r^2 = 0.6$ , Fig. A8). The dryness index exceeded 6 in only one year from 1959 to 1980, in five years from 1980 to 2001, and in six years from 2001 to 2022. This suggests an increase in the frequency of high dryness index episodes, indicating a rising frequency of summer droughts. Four years also stand out with particularly high dryness index values: 1989, 1994, 2003, and 2022, all of which occurred after the 1980s.

#### 4.4 Vegetation sensitivity

Figure 8 highlights the changes in the distribution of the annual cumulated Net Ecosystem Exchange (NEE) over 1959–2022. The black curve represents the probability density of NEE for a vegetation mix of 70 % herbaceous and 30 % *Sphagnum*, with shaded regions representing the 95 % confidence intervals accounting for variations in vegetation composition.

We observe that while the overall shape of the annual cumulative NEE probability density remains largely unchanged, significant differences arise depending on the vegetation type, particularly around the peak of the distributions. *Sphagnum* mosses amplify NEE extremes, either en-

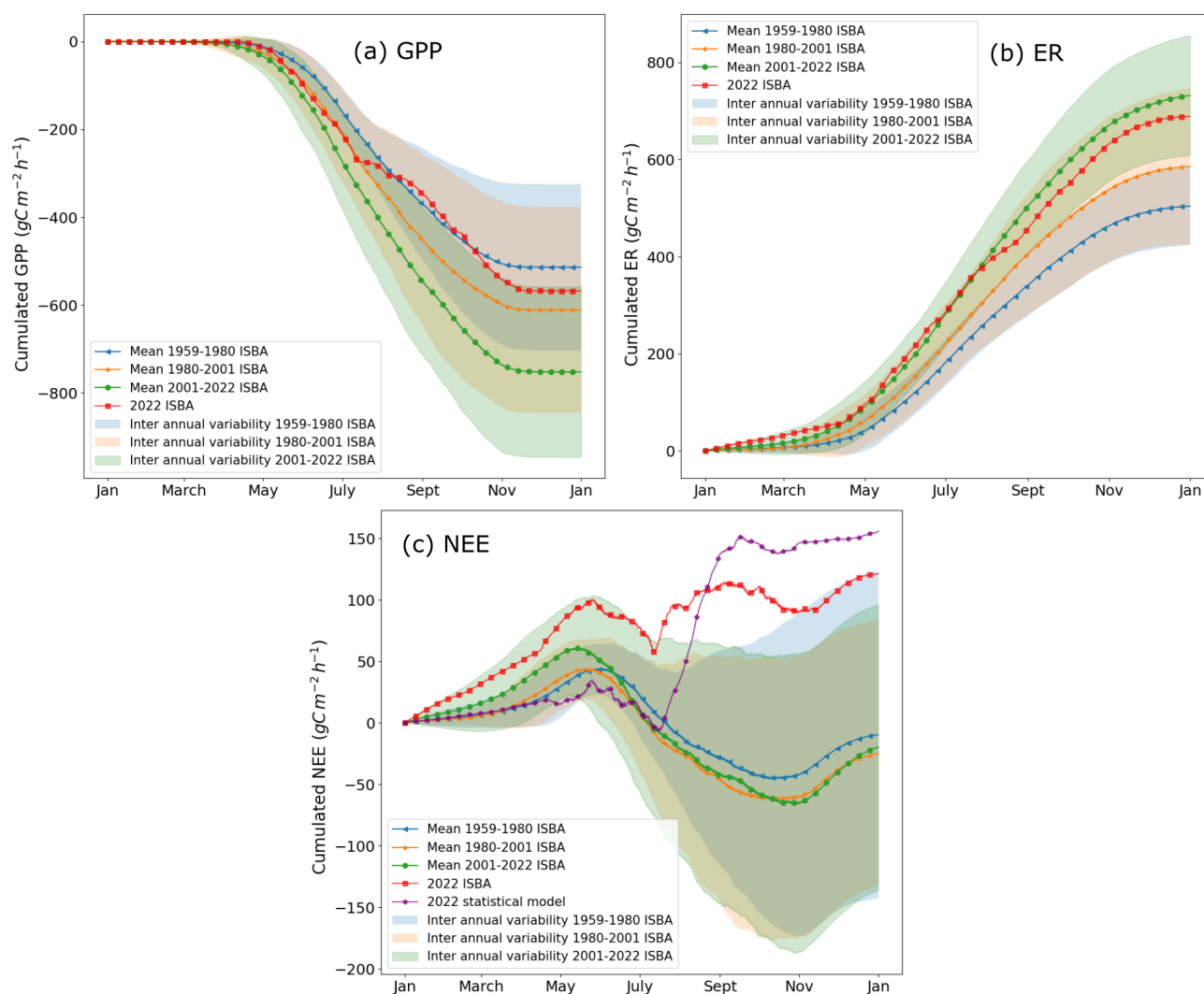


**Figure 5.** Seasonal evolution of cumulated (a) gross primary productivity (shown with negative sign by convention), (b) ecosystem respiration, (c) net ecosystem exchanges from ISBA over several time periods: 1959–1980 in blue, 1980–2001 in orange, 2001–2022 in green with interannual variability represented as a 90% confidence interval. Superimposed, the 2022 NEE seasonality simulated by ISBA (red curve) and the statistical model (purple curve).

hancing CO<sub>2</sub> absorption by vegetation or increasing CO<sub>2</sub> release to the atmosphere, resulting in a flatter distribution compared to herbaceous vegetation. In contrast, herbaceous plants have a buffering effect, with a distribution more concentrated around the main peak and a secondary, smaller peak slightly below +100 gC m<sup>-2</sup> yr<sup>-1</sup>, resulting in a bimodal pattern. These findings highlight the importance of considering different vegetation types, as they respond differently to changing environmental conditions. For completeness, the corresponding figures for GPP and ER are provided in the Appendix (Fig. A10).

## 5 Discussions

### 5.1 Model validation and vegetation sensitivity

The primary objective of this study was to evaluate the newly implemented *Sphagnum* PFT in the ISBA land surface model. *Sphagnum* photosynthetic activity is linked to water content in the top 10 cm of soil. While the model reproduces site scale carbon fluxes reasonably well given observational constraints, a more detailed validation of the water cycle would require eddy covariance data and multi site evaluations to assess parameter transferability. The aim was not to optimize parameters, but to test whether realistic behavior could be reproduced at a well instrumented site using literature derived values.

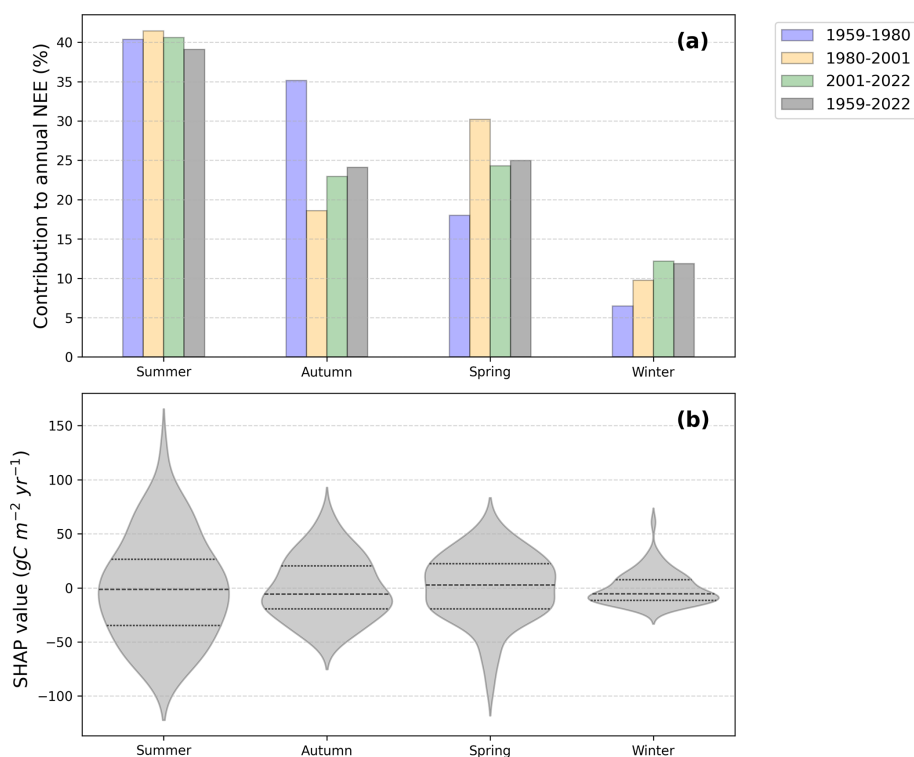


**Figure 6.** (a) Seasonal contributions to annual NEE across four time periods: 1959–1980 in blue, 1980–2001 in orange, 2001–2022 in green, 1959–2022 in grey. Each bar represents the relative importance of a season in explaining the total NEE, as determined by Shapley regression coefficients. Seasons are defined as winter (December–February), spring (March–June), summer (July–August), and autumn (September–November). (b) Distribution of SHAP values by season for 1959–2022. Positive or negative SHAP values indicate the direction of each season’s contribution to annual NEE, showing whether a season increases or decreases the yearly flux.

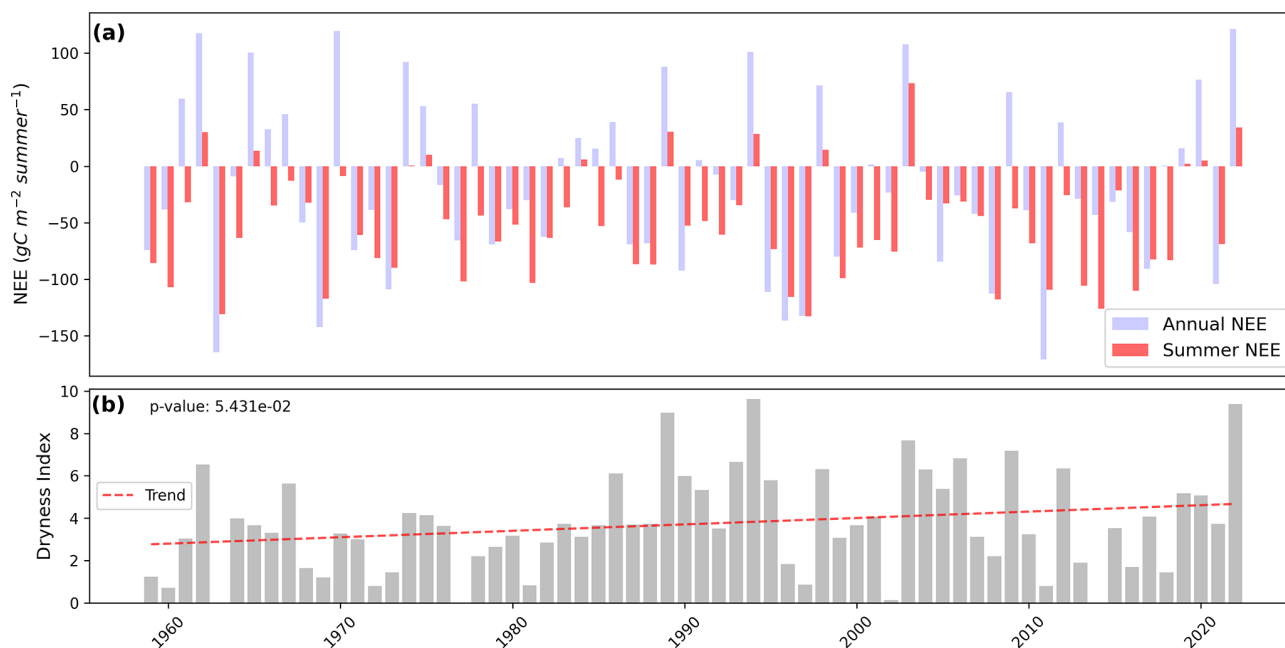


**Figure 7.** (a) Summer net ecosystem exchanges (in red) compared to annual (in blue) from 1959 to 2022, as simulated by ISBA. (b) Dryness index, derived from water table depth combining ISBA outputs and S2M reanalysis data, from 1959 to 2022 with its trend as red dashed line and associated  $p$  value.

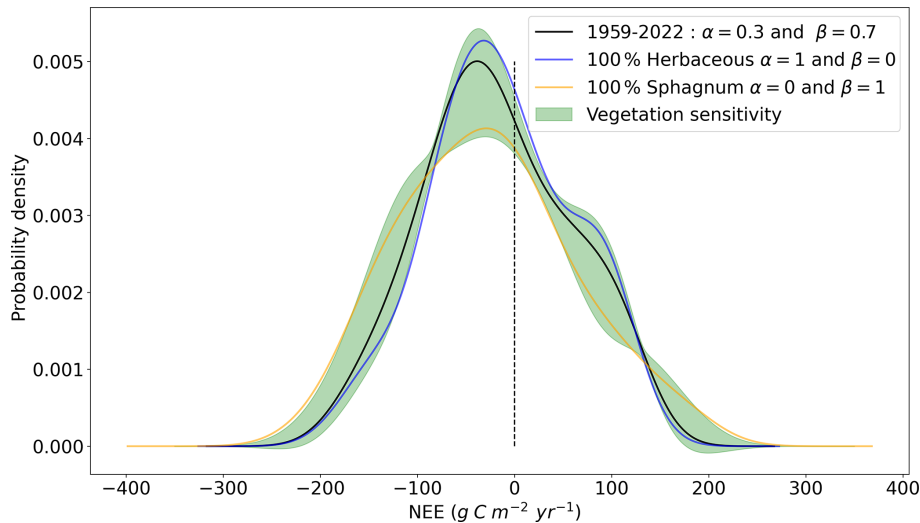


**Figure 8.** Probability density function of annual cumulated net ecosystem exchange over 1959–2022. In black, the vegetation mix corresponds to 70 % herbaceous and 30 % *Sphagnum*. In orange a 100 % *Sphagnum* mix and in blue a 100 % herbaceous mix. In shaded areas, the 95 % confidence intervals corresponding to the variation of the vegetation mix in the form  $\alpha \times NEE_{\text{Sphagnum}} + \beta \times NEE_{\text{herbaceous}}$  with  $\beta = 1 - \alpha$  and  $\alpha$  varying from 0 to 1 in steps of 0.01.

The mixed representation, combining *Sphagnum* and herbaceous PFTs, accounts for contrasting responses to soil moisture. We removed the influence of soil moisture on respiration ( $\theta(z)$ ) for *Sphagnum*, allowing the moss layer to maintain microbial activity under dry conditions, while it was retained for herbaceous layers to preserve the soil moisture sensitivity of heterotrophic respiration. Although respiration from the herbaceous component alone is not improved, retaining  $\theta(z)$  is consistent with previous validations of the ISBA model for herbaceous vegetation, ensuring the parameterization remains grounded in established formulations (Gibelin et al., 2008). Importantly, the combination of PFTs captures contrasting responses to soil moisture, introducing functional diversity that likely increases the robustness of ecosystem carbon fluxes. This mechanism is reflected in the observed modest improvement of NEE on the mixed vegetation dataset, even if GPP and respiration alone do not always show large gains. These results also highlight the broader uncertainty in representing heterotrophic respiration as a function of soil moisture: classical formulations derived from mineral soils may not adequately capture responses in organic soils, as noted in other peatland modeling studies (Qiu et al., 2019; Guenet et al., 2024), emphasizing the need for further research on moisture/respiration parameterizations.

By combining PFTs with contrasting functional responses, the model captures compensatory dynamics across vegetation types: herbaceous layers respond strongly to moisture deficits, while *Sphagnum* maintains near surface moisture and microbial activity. This functional diversity improves site scale carbon flux estimates and suggests increased model robustness under variable hydrological conditions, which could

be further enhanced by including interactive dynamics between *Sphagnum* mosses and herbaceous following the work of Kim and Verma (1996) but also competition and coupled carbon/water processes (Lippmann et al., 2023; Heijmans et al., 2008; Wu and Blodau, 2013a; Gong et al., 2020).

## 5.2 The key predictors of annual net ecosystem exchange (NEE)

The methodology developed in this study aimed to investigate the variability and evolution of carbon fluxes in the Bernadouze peatland from 1959 to 2022 using a CSM validated for the present period (2017–2022). This approach provides insight into the long-term functioning of the peatland on a century-scale timescale, which has been scarcely explored in the literature due to the lack of suitable tools. This novel methodology provides access to an unprecedented temporal scale, enabling current observations to be interpreted within a broader historical perspective.

Over the past 64 years, the Bernadouze peatland has shown marked variability in net ecosystem exchange (NEE), while overall maintaining its role as a carbon sink. This variability is strongly influenced by climatic and hydrological conditions, particularly precipitation, water table dynamics, and air temperature, as highlighted in previous research (Yurova et al., 2007; Laine et al., 2019). The reconstruction of water table height, together with the development of a dryness index that integrates both air temperature and water table depth, offers a robust explanation for the observed fluctuations in carbon fluxes, as also supported by other studies (Helbig et al., 2022). Vapor Pressure Deficit (VPD) is generally an important factor to consider, particularly for vegeta-

tion development, as it influences both GPP and plant transpiration (Fu et al., 2022). However, at the Bernadouze site, VPD is low and exhibits little variation (Figure A9 (a)), suggesting it has a limited effect on NEE. Furthermore, VPD is strongly correlated with temperature, which captures much of its potential influence. A recent study in Northern Hemisphere peatlands (Chen et al., 2023) also indicates that VPD has a neutral effect on vegetation and does not necessarily induce stomatal closure in vascular plants. The humid conditions at the site, along with the presence of bryophytes, help satisfy atmospheric water demand. Overall, air temperature and water table depth remain the primary drivers explaining NEE variability.

It is also observed that, in Bernadouze, summer NEE is the dominant contributor to the annual carbon balance, though the relative influence of other seasons varies across time periods. In recent decades, transitional seasons such as spring and autumn have become increasingly significant compared to earlier years. Understanding how climate change influences NEE seasonality offers key insight into the complex dynamics of carbon fluxes and the shifting balance between source and sink processes throughout the year, as also emphasized by Helbig et al. (2022). The dryness index developed in this study also appears to be a good proxy for summer NEE and, consequently, for annual NEE (Figs. A8 and A7). On other peatland sites where carbon flux measurements are not available, this index could potentially serve as a preliminary source of information to estimate the carbon balance of peatlands.

### 5.3 Climate change and droughts episode

Over the past 64 years, the Bernadouze peatland has experienced an increasing frequency of severe droughts, as indicated by the calculated dryness index (Figs. 7b and A3b). These events have contributed to the destabilization of the NEE balance, particularly in 2022. Despite some differences in seasonal representation, both ISBA and the statistical model by Garisoain et al. (2024) agree that from July to November 2022, conditions fell completely outside the range of interannual variability. Similar dry summers have occurred in the past, notably in 1989, 1994, and 2003, and have consistently led to significant CO<sub>2</sub> emissions into the atmosphere. The years 1989 and 2003 are recognized as having experienced different types of drought conditions in France, ranging from multi-year precipitation deficits (1989–1990) to short, hot, and dry periods (2003) (Vidal et al., 2010). Similarly, 1994 is also identified as a year with a hot summer, preceded by a winter precipitation deficit in Southern Europe (Vautard et al., 2007). The dryness index effectively captures these hot and dry summers, which impact vegetation, its development, and consequently, the NEE flux.

As the growing season lengthens and GPP increases due to rising air temperatures, a compensatory effect appears to be at play. The peatland's greening and higher summer GPP

fluxes currently help mitigate the impact of droughts, allowing it to remain a carbon sink. Over the 2001–2022 period, spring and autumn have played a growing role in shaping annual NEE, suggesting that these transitional seasons, along with winter, may become increasingly influential in the future, potentially counterbalancing summer carbon losses. However, the longevity of this balance remains uncertain. Some years, in our data, show a partial imbalance, indicating that the compensatory effect may not always fully buffer extreme conditions. Similar patterns have been observed in European forest ecosystems (van der Woude et al., 2023), where compensatory mechanisms were insufficient to maintain carbon balance; this provides a useful analogy for interpreting the partial signals we observe in our peatland data. While greening and seasonal compensation currently mitigate summer carbon losses, prolonged or intensified droughts in the future could challenge this balance and affect the peatland's long term carbon sink function.

The significant increase in annual maximum temperatures about 8 °C over 64 years raises concerns about the vegetation's ability to withstand such extreme warming. Studies on potential shifts in plant composition under climate change could provide valuable insights into the future of these ecosystems (Antala et al., 2022; Dieleman et al., 2015). This further emphasizes the need to integrate a broader range of plant communities and their interactions into land surface models, to more accurately represent ecosystem dynamics and their role in the carbon cycle.

## 6 Conclusion

This study highlights the importance of accurately representing *Sphagnum* mosses in land surface models to simulate peatland carbon dynamics under changing climatic conditions. Validation of the new *Sphagnum* PFT within the ISBA model showed its ability to reproduce observed carbon fluxes with reasonable agreement. Analysis of the Bernadouze peatland over the past 64 years revealed that while it has remained a net carbon sink, increasing drought frequency and severity, particularly exemplified by the 2022 event, are destabilizing its carbon balance. The findings emphasize the critical role of vegetation composition, hydrological conditions, and seasonal climate dynamics in modulating peatland carbon fluxes. They also suggest that although compensatory mechanisms currently maintain peatland sink function, future intensification of droughts driven by climate change could potentially shift these ecosystems from carbon sinks to carbon sources. This underscores the urgent need to integrate interactive vegetation dynamics and drought responses into land surface models to better project peatland contributions to the global carbon cycle under future climate scenarios.

## Appendix A: Figures and tables

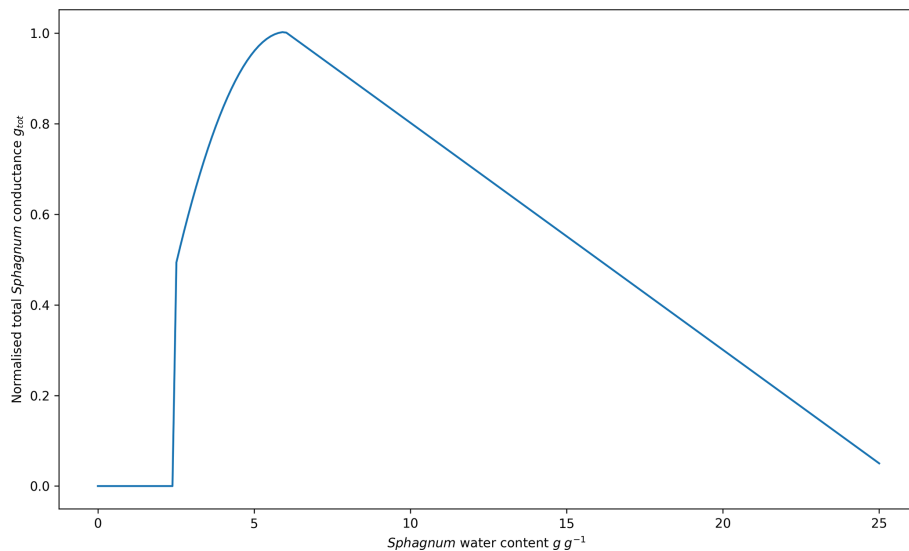


**Figure A1.** Normalised total Sphagnum conductance as a function of Sphagnum water content.

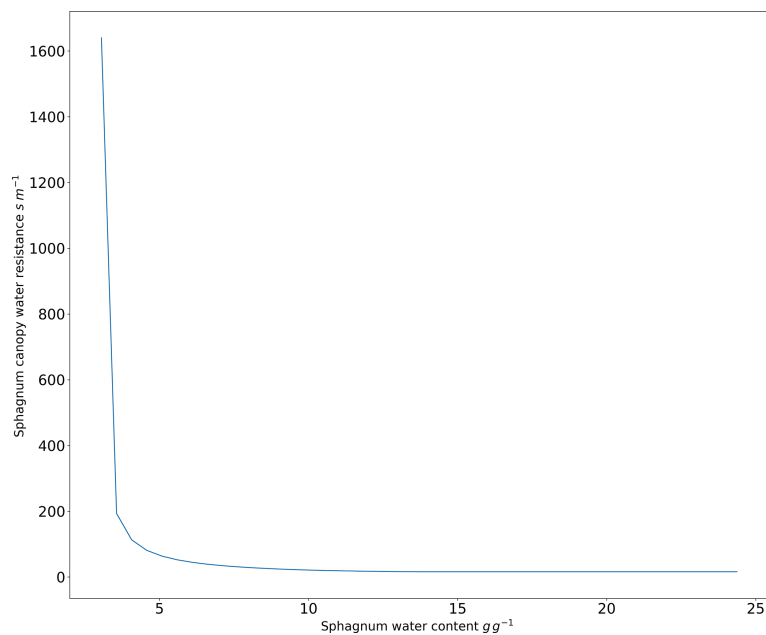


**Figure A2.** Sphagnum canopy water resistance as a function of Sphagnum water content.

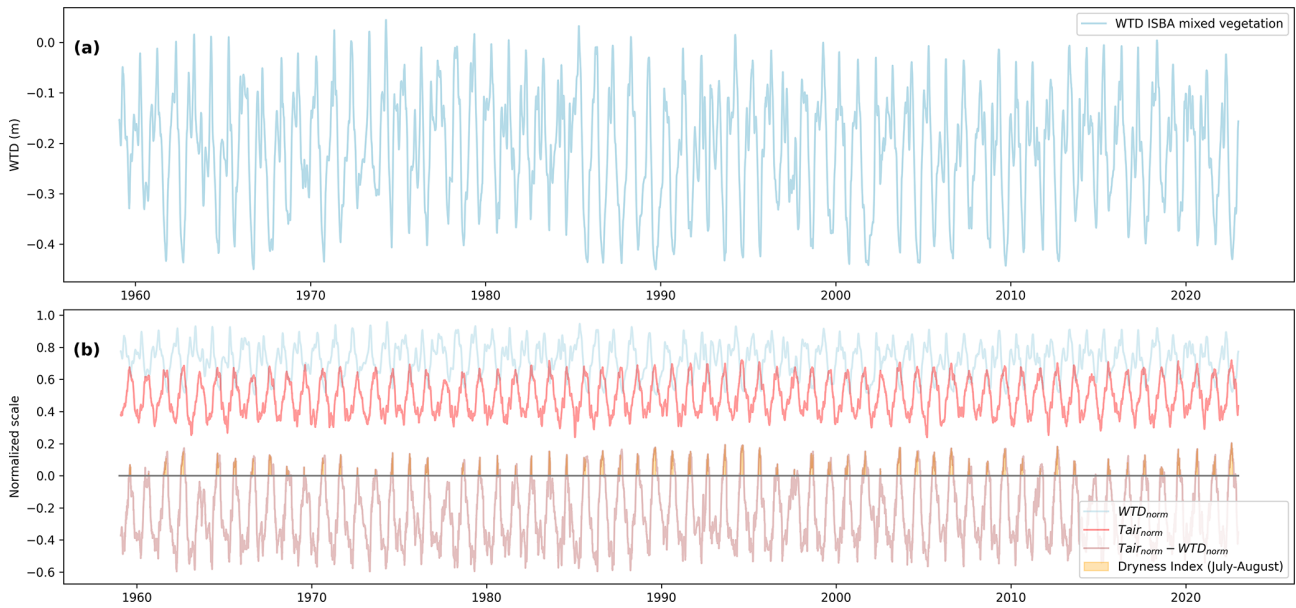


**Figure A3.** (a) Diagnosed water table depth (WTD) from 1959 to 2022 for the *Sphagnum*-herbaceous vegetation mix. (b) Light blue: normalized WTD, red: normalized air temperature ( $T_{air}$ ), pink: normalized  $T_{air}$  minus normalized WTD, dark blue area under the curve represents the dryness index (DI). Normalization of each variable ( $X$ ) was done following  $X_{normalized} = \frac{X - X_{min}}{X_{max} - X_{min}}$ .  $WTD_{min} = 1$  m is taken from observations and not the diagnosed one from ISBA.

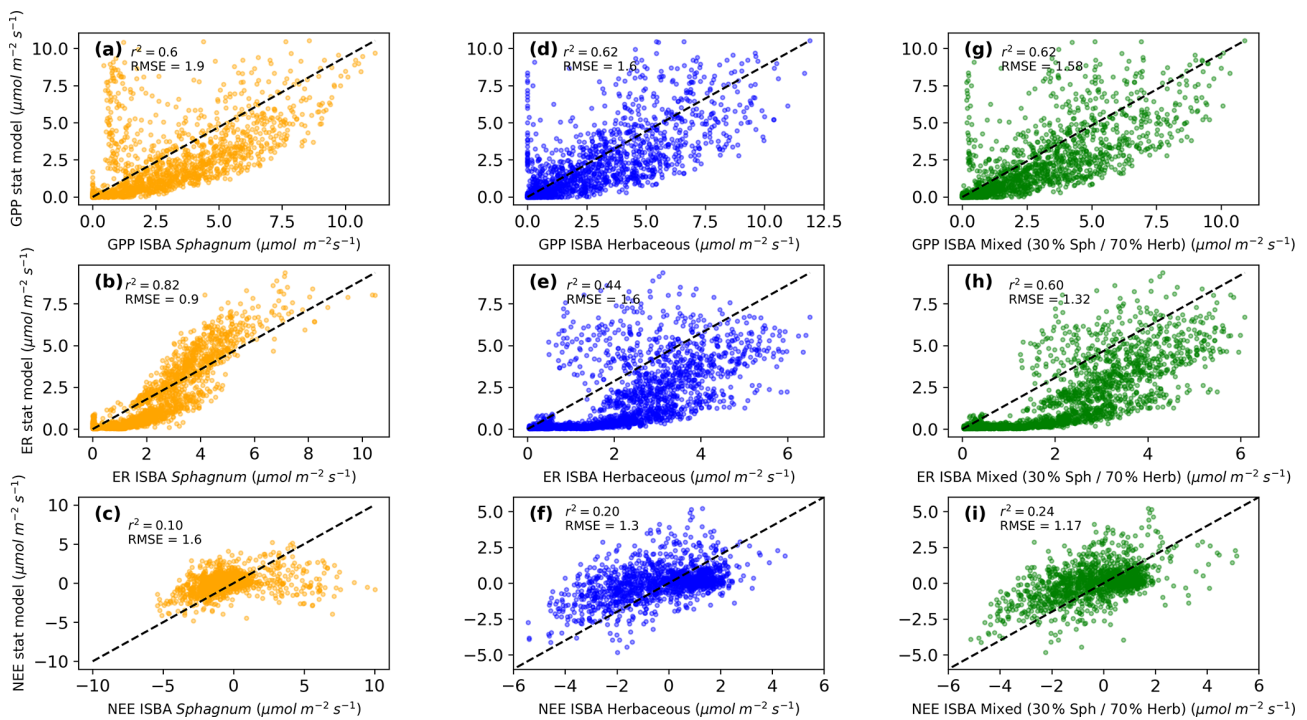


**Figure A4.** Comparison of daily ecosystem photosynthesis, respiration and net ecosystem exchange from the statistical model with: (a) the new *Sphagnum* photosynthesis, (b) the new *Sphagnum* ecosystem respiration, (c) the new *Sphagnum* net ecosystem exchange, (d) the previous herbaceous photosynthesis, (e) the previous herbaceous ecosystem respiration, (f) the previous herbaceous net ecosystem exchange, (g) the mixed vegetation photosynthesis, (h) the mixed vegetation ecosystem respiration, (i) the mixed vegetation net ecosystem exchange.

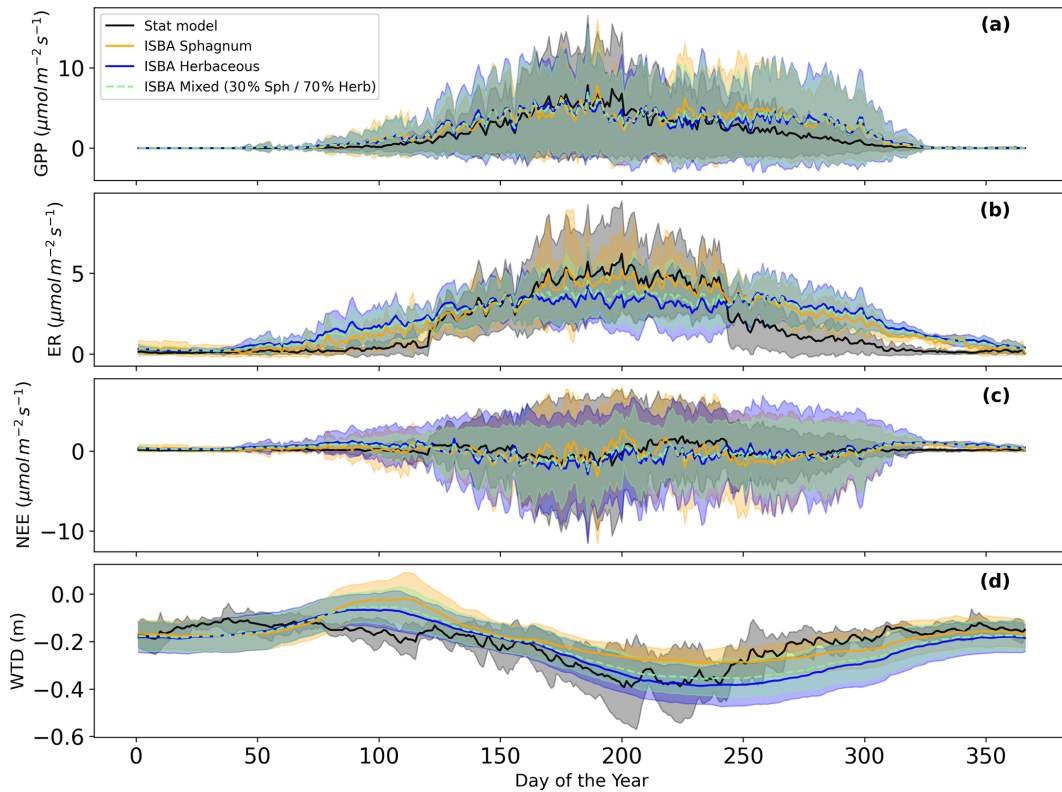


**Figure A5.** Daily annual cycle (2017–2022) of (a) Gross Primary Productivity, (b) Ecosystem Respiration, (c) Net Ecosystem Exchange, (d) Water Table Depth from the statistical model in black, the ISBA Sphagnum model in orange, the ISBA herbaceous model in blue, and the ISBA mixed vegetation in green.

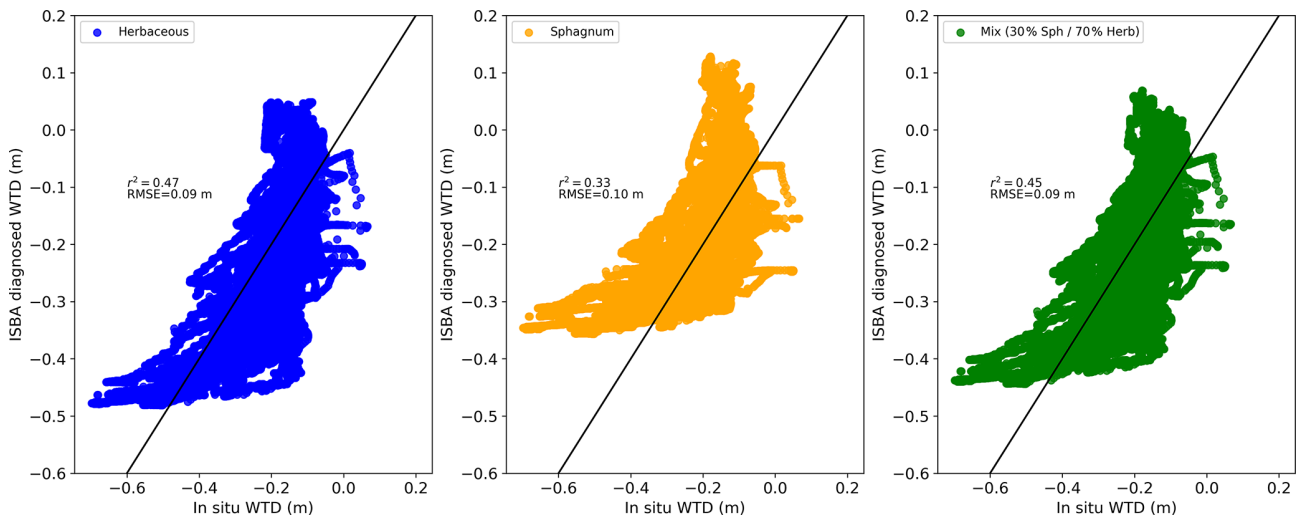


**Figure A6.** Hourly ISBA-diagnosed water table depth (WTD) with herbaceous vegetation as the dominant cover is compared to hourly in situ WTD in the left panel, while the right panel presents ISBA-diagnosed WTD with Sphagnum as the dominant vegetation versus in situ WTD.

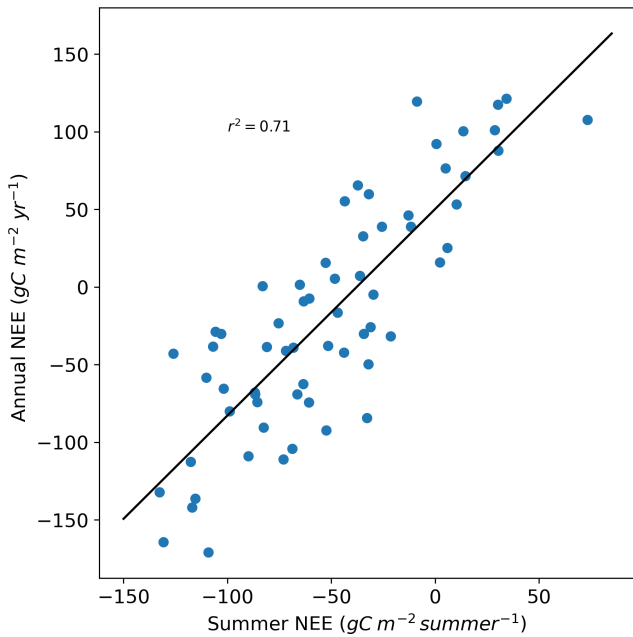


**Figure A7.** Annual NEE versus Summer NEE for each year from 1959 to 2022.

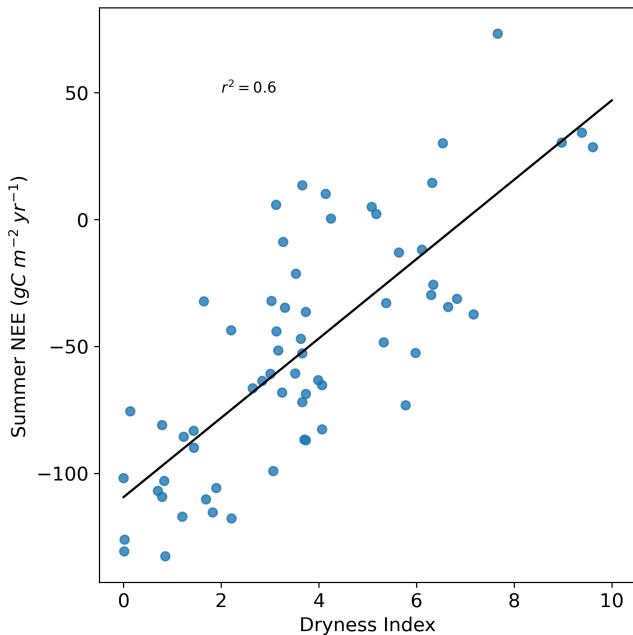


**Figure A8.** Summer NEE versus Dryness Index for each year from 1959 to 2022.

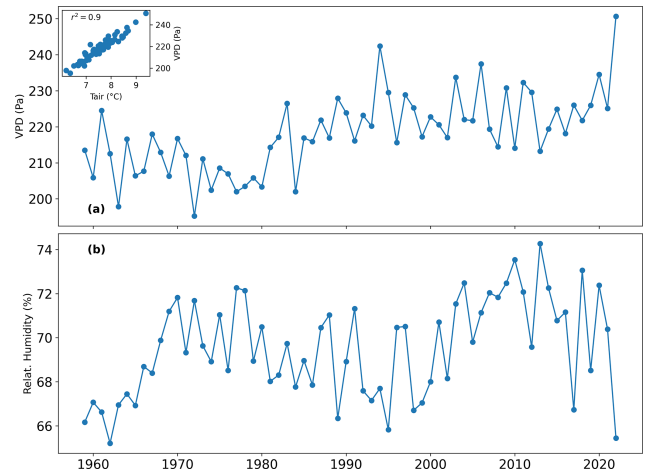


**Figure A9.** (a) Annual mean of vapor pressure deficit (VPD) (Pa) and scatter plot between VPD and air temperature; (b) Annual mean of relative humidity (%) from 1959 to 2022 derived from the S2M reanalysis.

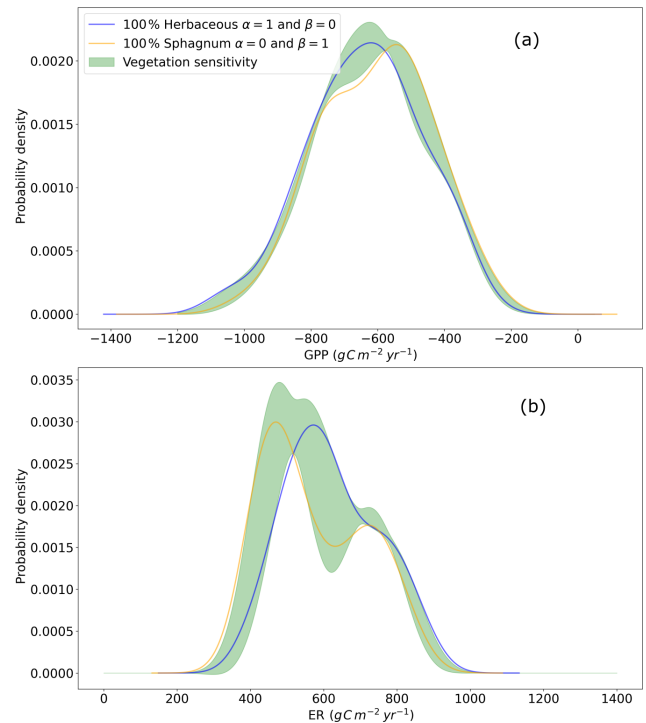


**Figure A10.** Probability density function of annual cumulated (a) GPP and (b) ER over 1959–2022. In black, the vegetation mix corresponds to 70 % herbaceous and 30 % Sphagnum. In orange a 100 % Sphagnum mix and in blue a 100 % herbaceous mix. In shaded areas, the 95 % confidence intervals corresponding to the variation of the vegetation mix in the form  $\alpha \times Y_{\text{Sphagnum}} + \beta \times Y_{\text{herbaceous}}$  with  $\beta = 1 - \alpha$ ,  $\alpha$  varying from 0 to 1 in steps of 0.01 and  $Y$  being GPP or ER.

**Table A1.** Changes between *Sphagnum* and C<sub>3</sub> herbaceous plant functional type in *ISBA*.

Parameters	Units	C <sub>3</sub> Herbaceous	Sphagnum	Comments
$\Gamma(25)$	ppmv	45	45	
$\epsilon_0$	kgCO <sub>2</sub> J <sup>-1</sup> PAR	$0.017 \times 10^{-6}$	$0.017 \times 10^{-6}$	
$Am_{\max}(25)$	mg m <sup>-2</sup> s <sup>-1</sup>	1.7	1.0	Jacob's hypothesis: $Am_{\max} = Vc_{\max}/2$ .
$f$	(-)	$f = f_0^*(1 - \frac{D_s}{D_{\max}^*}) + f_{\min} \frac{D_s}{D_{\max}^*}$	$f = f_0^*$	$f$ does not vary with air humidity
$f_0^*$	(-)	$f_0^* = 0.95$	$f_0^* = 0.8$	
$g_m$	m s <sup>-1</sup>	$g_m^* = e^{2.381 - 0.6103 \ln(D_{\max}^*)}$ $g_m = e^{2.381 - 0.6103 \ln(D_{\max})}$ $g_m = g_{m, \text{minimum}}$	$g_m = \alpha g_{\text{tot}}$ (Eq. 5) $g_m = \alpha g_{\text{tot}}$ (Eq. 5) $g_m = \alpha g_{\text{tot}}$ (Eq. 5)	SWI = 1 SWI <sub>c</sub> < SWI < 1 SWI ≤ SWI <sub>c</sub>
$D_{\max}$	kgH <sub>2</sub> O kg <sub>air</sub> <sup>-1</sup>	$D_{\max}^* = 0.045$ $D_{\max} = D_{\max}^X + (D_{\max}^* - D_{\max}^X) \frac{SWI - SWI_c}{1 - SWI_c}$ $D_{\max} = D_{\max}^X \frac{SWI}{SWI_c}$	Non used Non used Non used	SWI = 1 SWI <sub>c</sub> < SWI < 1 SWI ≤ SWI <sub>c</sub>
$\tau$	Days	150	80	
SLA	m <sup>2</sup> kg <sub>DryMass</sub> <sup>-1</sup>	$e = 5.56$ ; $f = 6.73$ ; $N_m = 1.3$	$e = 12$ ; $f = 5$ ; $N_m = 1.3$	
Root zone	-	20 cm, exponential profile distribution	no roots	Uniform distribution of <i>Sphagnum</i> over the top 10 cm
Vegetation height	m	$\frac{LAI}{6}$	0.05	Impacts Drag coefficient ( $H$ and $LE$ fluxes)

**Note 1:**  $g_m^*$ ,  $D_{\max}^*$  are the same quantities as  $g_m$ ,  $D_{\max}$  but without hydric stress. **Note 2:**  $D_{\max}^X = 0.4$ : this is the maximum value of  $D_{\max}$ .

**Table A2.** Parameters used for the *Sphagnum* PFT and their associated equations.

Parameter	Value	Equation
$\alpha$	0.0004 (mol <sup>-1</sup> m <sup>3</sup> )	(5)
$\beta$	-0.5	(4)
$\gamma$	0.5	(4)
$\eta$	-0.0416	(4)
$b$	27.6 (g g <sup>-1</sup> )	(11)
$c$	-0.5 (g g <sup>-1</sup> )	(11)
$d$	1 (s m <sup>-1</sup> )	(13)
$R_{s, \text{min}}$	$1e^{-4}$ m s <sup>-1</sup>	(13)
$w_{\text{min}}$	2.4 (g g <sup>-1</sup> )	(4)
$w_{\text{max}}$	22 (g g <sup>-1</sup> )	(4)
$w_{\text{opt}}$	6 (g g <sup>-1</sup> )	(4)

## Appendix B: ISBA equations

$$Am_{\max}(T_s) = \frac{Am_{\max}(25) \times Q_{10}^{(T_s-25)/10}}{[1 + \exp[0.3(T_1 - T_s)]] [1 + \exp[0.3(T_s - T_2)]]} \quad (\text{B1})$$

where  $Am_{\max}(25)$  is  $Am_{\max}$  at 25 °C,  $Q_{10}$  is fixed at 2.0,  $T_s$  is the skin temperature in °C and  $T_1$  and  $T_2$  are reference temperature values.  $gm$  in unstressed soil moisture conditions,  $gm^*$ , depends on temperature via the same  $Q_{10}$  function as  $Am_{\max}$ .

$$\Gamma(T_s) = \Gamma(25) \times Q_{10}^{(T_s-25)/10} \quad (\text{B2})$$

$\Gamma(25)$  is  $\Gamma$  at 25 °C. Here  $Q_{10}$  is fixed at 1.5.

$$\epsilon = \epsilon_0 \left( \frac{C_i - \Gamma}{C_i - 2\Gamma} \right) \quad (\text{B3})$$

$\epsilon$  is the initial quantum use efficiency, where  $\epsilon_0$  is the maximum quantum use efficiency.

$$C_i = fC_a + \Gamma(1 - f) \quad (\text{B4})$$

The internal  $CO_2$  concentration  $C_i$ , is directly derived from the  $CO_2$  concentration in the air  $C_a$  and from  $f$  which is detailed in Table A1.

$$\begin{aligned} E_g &= (1 - F_{\text{veg}}) \rho_a C_H V_a (\alpha q_{\text{sat}}(T_s) - q_a) \\ E_v &= F_{\text{veg}} \rho_a \left( \frac{\delta}{R_a} \right) (q_{\text{sat}}(T_s) - q_a) \\ E_{\text{tr}} &= F_{\text{veg}} \rho_a \left( \frac{1 - \delta}{R_a + R_s} \right) (q_{\text{sat}}(T_s) - q_a) \end{aligned} \quad (\text{B5})$$

The evaporation of the vegetated surface is the sum of the evaporation of the soil ( $E_g$ ) and the evaporation of the vegetation ( $E_{\text{veg}}$ ):  $E = E_g + E_{\text{veg}}$ . The evaporation of the vegetation is itself distributed between the direct evaporation ( $E_v$ ) due to the fraction of foliage covered by water intercepted and the transpiration ( $E_{\text{tr}}$ ):  $E_{\text{veg}} = E_v + E_{\text{tr}}$ .

$F_{\text{veg}}$  is the fraction of vegetation,  $\delta$  the fraction of foliage covered by intercepted water and  $R_s$  is the canopy resistance taking into account the upscaling of the cuticular and stomatal resistance.

For the modelling of *Sphagnum*,  $\delta$  is set to 0, and  $R_s$  is changed in  $R_{\text{sp}}$  (in this context, historical transpiration effectively corresponds to the evaporation from *Sphagnum*).

**Code and data availability.** The data presented in this study are available at <https://doi.org/10.5281/zenodo.16984992> (Garisoain et al., 2025).

The S2M dataset is freely accessible via the AERIS data center at <https://doi.org/10.25326/37#v2020.2> (Vernay et al., 2023). The S2M data are provided by Météo-France, CNRS, CNRM, and the Centre d'Études de la Neige through AERIS.

The model used in this study is open-source. The ISBA model, as implemented in this work, is part of SURFEX version 9 and can be downloaded from the SURFEX platform: <http://www.umr-cnrm.fr/surfex/> (last access: 11 May 2026).

**Author contributions.** RG, CD, BD and LG conceptualized and designed the study. RG modified and implemented the model, conducted formal analysis of the results, and led the writing of the original draft with contributions from all co-authors. All authors participated in reviewing, editing, and finalizing the manuscript.

**Competing interests.** The contact author has declared that none of the authors has any competing interests.

**Disclaimer.** Publisher's note: Copernicus Publications remains neutral with regard to jurisdictional claims made in the text, published maps, institutional affiliations, or any other geographical representation in this paper. The authors bear the ultimate responsibility for providing appropriate place names. Views expressed in the text are those of the authors and do not necessarily reflect the views of the publisher.

**Acknowledgements.** The authors gratefully acknowledge Matthieu Lafaysse for providing the S2M data and for his valuable support.

**Financial support.** This work is part of project PEACE of the exploratory research program FairCarboN and received government funding managed by the Agence Nationale de la Recherche under the France 2030 program, reference ANR-22-PEXF-0011. Observatoire Homme-Milieu Pyrenees Haut Vicdessos – LABEX DRI-IHM ANR-11-LABX0010. The bernadouze site is part of the “Service National d’Observation des Tourbières” (SNO-French Peatland Observatory), part of the research infrastructure OZCAR, accredited by the INSU/CNRS.

**Review statement.** This paper was edited by Petr Kuneš and reviewed by Katharina Jentsch and one anonymous referee.

## References

- Antala, M., Juszczak, R., van der Tol, C., and Rastogi, A.: Impact of climate change-induced alterations in peatland vegetation phenology and composition on carbon balance, *Sci. Total Environ.*, 827, 154294, <https://doi.org/10.1016/j.scitotenv.2022.154294>, 2022.
- Bond-Lamberty, B., Gower, S. T., Amiro, B., and Ewers, B. E.: Measurement and modelling of bryophyte evaporation in a boreal forest chronosequence, *Ecophysiology*, 4, 26–35, <https://doi.org/10.1002/eco.118>, 2011.
- Boone, A. and Etchevers, P.: An Intercomparison of Three Snow Schemes of Varying Complexity Coupled to the Same Land Surface Model: Local-Scale Evaluation at an Alpine Site, *J. Hydrometeorol.*, 2, 374–394, [https://doi.org/10.1175/1525-7541\(2001\)002<0374:AIOTSS>2.0.CO;2](https://doi.org/10.1175/1525-7541(2001)002<0374:AIOTSS>2.0.CO;2), 2001.

- Bunsen, M. S. and Loisel, J.: Carbon storage dynamics in peatlands: Comparing recent- and long-term accumulation histories in southern Patagonia, *Glob. Change Biol.*, 26, 5778–5795, <https://doi.org/10.1111/gcb.15262>, 2020.
- Calvet, J.-C. and Soussana, J.-F.: Modelling CO<sub>2</sub>-enrichment effects using an interactive vegetation SVAT scheme, *Agr. Forest Meteorol.*, 108, 129–152, [https://doi.org/10.1016/S0168-1923\(01\)00235-0](https://doi.org/10.1016/S0168-1923(01)00235-0), 2001.
- Carrer, D., Roujean, J.-L., Lafont, S., Calvet, J.-C., Boone, A., Decharme, B., Delire, C., and Gastellu-Etchegorry, J.-P.: A canopy radiative transfer scheme with explicit FA- PAR for the interactive vegetation model ISBA-A-gs: Impact on carbon fluxes, *J. Geophys. Res.-Biogeo.*, 118, 888–903, <https://doi.org/10.1002/jgrg.20070>, 2013.
- Carter, M. S., Larsen, K. S., Emmett, B., Estiarte, M., Field, C., Leith, I. D., Lund, M., Meijide, A., Mills, R. T. E., Ninemets, Ü., Peñuelas, J., Portillo-Estrada, M., Schmidt, I. K., Selsted, M. B., Sheppard, L. J., Sowerby, A., Tietema, A., and Beier, C.: Synthesizing greenhouse gas fluxes across nine European peatlands and shrublands – responses to climatic and environmental changes, *Biogeosciences*, 9, 3739–3755, <https://doi.org/10.5194/bg-9-3739-2012>, 2012.
- Chadburn, S., Burke, E., Essery, R., Boike, J., Langer, M., Heikenfeld, M., Cox, P., and Friedlingstein, P.: An improved representation of physical permafrost dynamics in the JULES land-surface model, *Geosci. Model Dev.*, 8, 1493–1508, <https://doi.org/10.5194/gmd-8-1493-2015>, 2015.
- Chaudhary, N., Miller, P. A., and Smith, B.: Modelling past, present and future peatland carbon accumulation across the pan-Arctic region, *Biogeosciences*, 14, 4023–4044, <https://doi.org/10.5194/bg-14-4023-2017>, 2017.
- Chen, N., Zhang, Y., Yuan, F., Song, C., Xu, M., Wang, Q., Hao, G., Bao, T., Zuo, Y., Liu, J., Zhang, T., Song, Y., Sun, L., Guo, Y., Zhang, H., Ma, G., Du, Y., Xu, X., and Wang, X.: Warming-Induced Vapor Pressure Deficit Suppression of Vegetation Growth Diminished in Northern Peatlands, *Nat. Commun.*, 14, 7885, <https://doi.org/10.1038/s41467-023-42932-w>, 2023.
- Clymo, R. S. and Hayward, P. M.: The Ecology of *Sphagnum*, in: *Bryophyte Ecology*, edited by: Smith, A. J. E., 229–289, Springer Netherlands, [https://doi.org/10.1007/978-94-009-5891-3\\_8](https://doi.org/10.1007/978-94-009-5891-3_8), 1982.
- Collatz, G. J., Ribas-Carbo, M., and Berry, J. A.: Coupled Photosynthesis-Stomatal Conductance Model for Leaves of C<sub>4</sub> Plants, *Functional Plant Biology*, 19, 519–538, <https://doi.org/10.1071/pp9920519>, 1992.
- Decharme, B., Brun, E., Boone, A., Delire, C., Le Moigne, P., and Morin, S.: Impacts of snow and organic soils parameterization on northern Eurasian soil temperature profiles simulated by the ISBA land surface model, *The Cryosphere*, 10, 853–877, <https://doi.org/10.5194/tc-10-853-2016>, 2016.
- Delire, C., Séférian, R., Decharme, B., Alkama, R., Calvet, J.-C., Carrer, D., Gibelin, A.-L., Joetzjer, E., Morel, X., Rocher, M., and Tzanos, D.: The Global Land Carbon Cycle Simulated With ISBA-CTRIP: Improvements Over the Last Decade, *J. Adv. Model. Earth Sy.*, 12, e2019MS001886, <https://doi.org/10.1029/2019MS001886>, 2020.
- Dieleman, C. M., Branfireun, B. A., McLaughlin, J. W., and Lindo, Z.: Climate change drives a shift in peatland ecosystem plant community: Implications for ecosystem function and stability, *Glob. Change Biol.*, 21, 388–395, <https://doi.org/10.1111/gcb.12643>, 2015.
- Druel, A., Peylin, P., Krinner, G., Ciais, P., Viovy, N., Peregon, A., Bastrikov, V., Kosykh, N., and Mironycheva-Tokareva, N.: Towards a more detailed representation of high-latitude vegetation in the global land surface model ORCHIDEE (ORC-HL-VEGv1.0), *Geosci. Model Dev.*, 10, 4693–4722, <https://doi.org/10.5194/gmd-10-4693-2017>, 2017.
- Faranda, D., Pascale, S., and Bulut, B.: Persistent anticyclonic conditions and climate change exacerbated the exceptional 2022 European-Mediterranean drought, *Environ. Res. Lett.*, 18, <https://doi.org/10.1088/1748-9326/acbc37>, 2023.
- Frolking, S., Roulet, N. T., Tuittila, E., Bubier, J. L., Quillet, A., Talbot, J., and Richard, P. J. H.: A new model of Holocene peatland net primary production, decomposition, water balance, and peat accumulation, *Earth Syst. Dynam.*, 1, 1–21, <https://doi.org/10.5194/esd-1-1-2010>, 2010.
- Frolking, S., Talbot, J., and Subin, Z. M.: Exploring the relationship between peatland net carbon balance and apparent carbon accumulation rate at century to millennial time scales, *The Holocene*, 24, 1167–1173, 2014.
- Fu, Z., Ciais, P., Prentice, I. C., Gentine, P., Makowski, D., Bastos, A., Luo, X., Green, J. K., Stoy, P. C., Yang, H., and Hajima, T.: Atmospheric Dryness Reduces Photosynthesis along a Large Range of Soil Water Deficits, *Nat. Commun.*, 13, 989, <https://doi.org/10.1038/s41467-022-28652-7>, 2022.
- Garisoain, R., Delire, C., Decharme, B., Ferrant, S., Granouillac, F., Payre-Suc, V., and Gandois, L.: A Study of Dominant Vegetation Phenology in a *Sphagnum* Mountain Peatland Using In Situ and Sentinel-2 Observations, *J. Geophys. Res.-Biogeo.*, 128, e2023JG007403, <https://doi.org/10.1029/2023JG007403>, 2023.
- Garisoain, R., Jacotot, A., Delire, C., Binet, S., Le Roux, G., Gascoin, S., Rosset, T., Gogo, S., Granouillac, F., Payre-Suc, V., and Gandois, L.: Mountain Peatlands and Drought: Carbon Cycling in the Pyrenees Amidst Global Climate Change, *J. Geophys. Res.-Biogeo.*, 129, e2024JG008041, <https://doi.org/10.1029/2024JG008041>, 2024.
- Garisoain, R., Delire, C., Decharme, B., and gandois, l.: *Sphagnum* and Herbaceous Net Ecosystem Exchanges in a Pyrenean Peatland: A Long-Term Study Using the ISBA Model, Zenodo [dataset], <https://doi.org/10.5281/zenodo.16984992>, 2025.
- Gibelin, A.-L., Calvet, J.-C., and Viovy, N.: Modelling energy and CO<sub>2</sub> fluxes with an interactive vegetation land surface model-Evaluation at high and middle latitudes, *Agr. Forest Meteorol.*, 148, 1611–1628, <https://doi.org/10.1016/j.agrformet.2008.05.013>, 2008.
- Gong, J., Roulet, N., Frolking, S., Peltola, H., Laine, A. M., Kokkonen, N., and Tuittila, E.-S.: Modelling the habitat preference of two key *Sphagnum* species in a poor fen as controlled by capitulum water content, *Biogeosciences*, 17, 5693–5719, <https://doi.org/10.5194/bg-17-5693-2020>, 2020.
- Gorham, E., Lehman, C., Dyke, A., Clymo, D., and Janssens, J.: Long-term carbon sequestration in North American peatlands, *Quaternary Sci. Rev.*, 58, 77–82, <https://doi.org/10.1016/j.quascirev.2012.09.018>, 2012.

- Goudriaan, J.: A simple and fast numerical method for the computation of daily totals of crop photosynthesis, *Agr. Forest Meteorol.*, 38, 249–254, [https://doi.org/10.1016/0168-1923\(86\)90063-8](https://doi.org/10.1016/0168-1923(86)90063-8), 1986.
- Grant, R. F., Desai, A. R., and Sulman, B. N.: Modelling contrasting responses of wetland productivity to changes in water table depth, *Biogeosciences*, 9, 4215–4231, <https://doi.org/10.5194/bg-9-4215-2012>, 2012.
- Guenet, B., Eglin, T., Vasilyeva, N., Peylin, P., Ciais, P., and Chenu, C.: The relative importance of decomposition and transport mechanisms in accounting for soil organic carbon profiles, *Biogeosciences*, 10, 2379–2392, <https://doi.org/10.5194/bg-10-2379-2013>, 2013.
- Guenet, B., Orliac, J., Cécillon, L., Torres, O., Sereni, L., Martin, P. A., Barré, P., and Bopp, L.: Spatial biases reduce the ability of Earth system models to simulate soil heterotrophic respiration fluxes, *Biogeosciences*, 21, 657–669, <https://doi.org/10.5194/bg-21-657-2024>, 2024.
- Helbig, M., Živković, T., Alekseychik, P., Aurela, M., El-Madany, T. S., Euskirchen, E. S., Flanagan, L. B., Griffis, T. J., Hanson, P. J., Hattakka, J., Helfter, C., Hirano, T., Humphreys, E. R., Kiely, G., Kolka, R. K., Laurila, T., Leahy, P. G., Lohila, A., Mammarella, I., Nilsson, M. B., Panov, A., Parmentier, F. J. W., Peichl, M., Rinne, J., Roman, D. T., Sonnentag, O., Tuittila, E.-S., Ueyama, M., Vesala, T., Vestin, P., Weldon, S., Weslien, P., and Zaehle, S.: Warming Response of Peatland CO<sub>2</sub> Sink Is Sensitive to Seasonality in Warming Trends, *Nat. Clim. Change*, 12, 743–749, <https://doi.org/10.1038/s41558-022-01428-z>, 2022.
- Henry, E., Infante Sanchez, M., and Corriol, G.: *Tourbière de Bernadouze (Suc-et-Sentenac, 09). Expérimentation d'une cartographie fine des végétations*, Tech. rep., Conservatoire botanique national des Pyrénées et de Midi-Pyrénées, Bagnères de Bigorre, 2014.
- Jacobs, C.: Direct impact of atmospheric CO<sub>2</sub> enrichment on regional transpiration, PhD Theses, Wageningen, ISBN 90-5485-250-X, 1994.
- Jacobs, C. M. J., van den Hurk, B. M. M., and de Bruin, H. A. R.: Stomatal behaviour and photosynthetic rate of unstressed grapevines in semi-arid conditions, *Agr. Forest Meteorol.*, 80, 111–134, [https://doi.org/10.1016/0168-1923\(95\)02295-3](https://doi.org/10.1016/0168-1923(95)02295-3), 1996.
- Kim, J. and Verma, S. B.: Surface Exchange of Water Vapour between an Open Sphagnum Fen and the Atmosphere, *Bound.-Lay. Meteorol.*, 79, 243–264, <https://doi.org/10.1007/BF00119440>, 1996.
- Koven, C., Friedlingstein, P., Ciais, P., Khvorostyanov, D., Krinner, G., and Tarnocai, C.: On the formation of high-latitude soil carbon stocks: Effects of cryoturbation and insulation by organic matter in a land surface model, *Geophys. Res. Lett.*, 36, <https://doi.org/10.1029/2009GL040150>, 2009.
- Laine, A. M., Mäkiranta, P., Laiho, R., Mehtätalo, L., Penttilä, T., Korrensalo, A., Minkkinen, K., Fritze, H., and Tuittila, E.-S.: Warming impacts on boreal fen CO<sub>2</sub> exchange under wet and dry conditions, *Glob. Change Biol.*, 25, 1995–2008, <https://doi.org/10.1111/gcb.14617>, 2019.
- Lang, S. I., Cornelissen, J. H. C., Klahn, T., Van Logtestijn, R. S. P., Broekman, R., Schweikert, W., and Aerts, R.: An Experimental Comparison of Chemical Traits and Litter Decomposition Rates in a Diverse Range of Subarctic Bryophyte, Lichen and Vascular Plant Species, *J. Ecol.*, 97, 886–900, <https://doi.org/10.1111/j.1365-2745.2009.01538.x>, 2009.
- Loisel, J. and Yu, Z.: Recent acceleration of carbon accumulation in a boreal peatland, south central Alaska, *J. Geophys. Res.-Biogeo.*, 118, 41–53, <https://doi.org/10.1029/2012JG001978>, 2013.
- Loisel, J., Gallego-Sala, A. V., Amesbury, M. J., Magnan, G., Anshari, G., Beilman, D. W., Benavides, J. C., Blewett, J., Camill, P., Charman, D. J., Chawchai, S., Hedgpeth, A., Kleinen, T., Korhola, A., Large, D., Mansilla, C. A., Muller, J., van Bellen, S., West, J. B., Yu, Z., Bubier, J. L., Garneau, M., Moore, T., Sannel, A. B. K., Page, S., Valiranta, M., Bechtold, M., Brovkin, V., Cole, L. E. S., Chanton, J. P., Christensen, T. R., Davies, M. A., De Vleeschouwer, F., Finkelstein, S. A., Froking, S., Galka, M., Gandois, L., Girkin, N., Harris, L. I., Heinemeyer, A., Hoyt, A. M., Jones, M. C., Joos, F., Juutinen, S., Kaiser, K., Lacourse, T., Lamentowicz, M., Larmola, T., Leifeld, J., Lohila, A., Milner, A. M., Minkkinen, K., Moss, P., Naafs, B. D. A., Nichols, J., O'Donnell, J., Payne, R., Philben, M., Piilo, S., Quillet, A., Ratnayake, A. S., Roland, T. P., Sjögersten, S., Sonnentag, O., Swindles, G. T., Swinnen, W., Talbot, J., Treat, C., Valach, A. C., and Wu, J.: Expert assessment of future vulnerability of the global peatland carbon sink, *Nat. Clim. Change*, 11, 70–77, <https://doi.org/10.1038/s41558-020-00944-0>, 2021.
- Metzger, C., Nilsson, M. B., Peichl, M., and Jansson, P.-E.: Parameter interactions and sensitivity analysis for modelling carbon heat and water fluxes in a natural peatland, using CoupModel v5, *Geosci. Model Dev.*, 9, 4313–4338, <https://doi.org/10.5194/gmd-9-4313-2016>, 2016.
- Morel, X., Decharme, B., Delire, C., Krinner, G., Lund, M., Hansen, B. U., and Mastepanov, M.: A New Process-Based Soil Methane Scheme: Evaluation Over Arctic Field Sites With the ISBA Land Surface Model, *J. Adv. Model. Earth Sy.*, 11, 293–326, <https://doi.org/10.1029/2018MS001329>, 2019.
- Packalen, M. S. and Finkelstein, S. A.: Quantifying Holocene variability in carbon uptake and release since peat initiation in the Hudson Bay Lowlands, Canada, *The Holocene*, 24, 1063–1074, <https://doi.org/10.1177/0959683614540728>, 2014.
- Page, S. and Baird, A.: Peatlands and Global Change: Response and Resilience, *Annu. Rev. Env. Resour.*, 41, 35–57, <https://doi.org/10.1146/annurev-environ-110615-085520>, 2016.
- Park, H., Launiainen, S., Konstantinov, P. Y., Iijima, Y., and Fedorov, A. N.: Modeling the Effect of Moss Cover on Soil Temperature and Carbon Fluxes at a Tundra Site in Northeastern Siberia, *J. Geophys. Res.-Biogeo.*, 123, 3028–3044, <https://doi.org/10.1029/2018JG004491>, 2018.
- Parton, W. J., Scurlock, J. M. O., Ojima, D. S., Gilmanov, T. G., Scholes, R. J., Schimel, D. S., Kirchner, T., Menaut, J.-C., Seastedt, T., Garcia Moya, E., Kamnalrut, A., and Kinyamario, J. I.: Observations and Modeling of Biomass and Soil Organic Matter Dynamics for the Grassland Biome Worldwide, *Glob. Biogeochem. Cycles*, 7, 785–809, <https://doi.org/10.1029/93GB02042>, 1993.
- Porada, P., Ekici, A., and Beer, C.: Effects of bryophyte and lichen cover on permafrost soil temperature at large scale, *The Cryosphere*, 10, 2291–2315, <https://doi.org/10.5194/tc-10-2291-2016>, 2016.
- Qiu, C., Zhu, D., Ciais, P., Guenet, B., Peng, S., Krinner, G., Tootchi, A., Ducharme, A., and Hastie, A.: Modelling northern peatland area and carbon dynamics since the Holocene with the

- ORCHIDEE-PEAT land surface model (SVN r5488), *Geosci. Model Dev.*, 12, 2961–2982, <https://doi.org/10.5194/gmd-12-2961-2019>, 2019.
- Robroek, B. J. M., Devilee, G., Telgenkamp, Y., Härlin, C., Steele, M. N., Barel, J. M., and Lamers, L. P. M.: More is not always better: peat moss mixtures slightly enhance peatland stability, *P. R. Soc. B*, 291, 20232622, <https://doi.org/10.1098/rspb.2023.2622>, 2024.
- Rogora, M., Frate, L., Carranza, M. L., Freppaz, M., Stanisci, A., Bertani, I., Bottarin, R., Brambilla, A., Canullo, R., Carbognani, M., Cerrato, C., Chelli, S., Cremonese, E., Cutini, M., Di Musciano, M., Erschbamer, B., Godone, D., Iocchi, M., Isabellon, M., Magnani, A., Mazzola, L., Morra di Cella, U., Pauli, H., Petey, M., Petriccione, B., Porro, F., Psenner, R., Rossetti, G., Scotti, A., Sommaruga, R., Tappeiner, U., Theurillat, J. P., Tomaselli, M., Viglietti, D., Viterbi, R., Vittoz, P., Winkler, M., and Matteucci, G.: Assessment of climate change effects on mountain ecosystems through a cross-site analysis in the Alps and Apennines, *Sci. Total Environ.*, 624, 1429–1442, <https://doi.org/10.1016/j.scitotenv.2017.12.155>, 2018.
- Scheffer, R. A., Van Logtestijn, R. S. P., and Verhoeven, J. T. A.: Decomposition of *Carex* and *Sphagnum* Litter in Two Mesotrophic Fens Differing in Dominant Plant Species, *Oikos*, 92, 44–54, <https://doi.org/10.1034/j.1600-0706.2001.920106.x>, 2001.
- Shi, X., Thornton, P. E., Ricciuto, D. M., Hanson, P. J., Mao, J., Sebestyen, S. D., Griffiths, N. A., and Bisht, G.: Representing northern peatland microtopography and hydrology within the Community Land Model, *Biogeosciences*, 12, 6463–6477, <https://doi.org/10.5194/bg-12-6463-2015>, 2015.
- Shi, X., Ricciuto, D. M., Thornton, P. E., Xu, X., Yuan, F., Norby, R. J., Walker, A. P., Warren, J. M., Mao, J., Hanson, P. J., Meng, L., Weston, D., and Griffiths, N. A.: Extending a land-surface model with *Sphagnum* moss to simulate responses of a northern temperate bog to whole ecosystem warming and elevated CO<sub>2</sub>, *Biogeosciences*, 18, 467–486, <https://doi.org/10.5194/bg-18-467-2021>, 2021.
- Sterk, H. P., Marshall, C., Cowie, N. R., Clutterbuck, B., McIlvenny, J., and Andersen, R.: Blanket bog CO<sub>2</sub> flux driven by plant functional type during summer drought, *Ecohydrology*, 16, e2503, <https://doi.org/10.1002/eco.2503>, 2023.
- St-Hilaire, F., Wu, J., Roulet, N. T., Frolking, S., Lafleur, P. M., Humphreys, E. R., and Arora, V.: McGill wetland model: evaluation of a peatland carbon simulator developed for global assessments, *Biogeosciences*, 7, 3517–3530, <https://doi.org/10.5194/bg-7-3517-2010>, 2010.
- Turetsky, M. R.: The Role of Bryophytes in Carbon and Nitrogen Cycling, *The Bryologist*, 106, 395–409, <https://doi.org/10.1639/05>, 2003.
- Turunen, J.: Past and present carbon accumulation in undisturbed boreal and subarctic mires: A review, *Suo*, 54, 15–28, 2003.
- van der Woude, A. M., Peters, W., Joetzier, E., Lafont, S., Koren, G., Ciais, P., Ramonet, M., Xu, Y., Bastos, A., Botia, S., Sitch, S., de Kok, R., Kneuer, T., Kubistin, D., Jacotot, A., Loubet, B., Herig-Coimbra, P.-H., Loustau, D., and Luijkx, I. T.: Temperature extremes of 2022 reduced carbon uptake by forests in Europe, *Nat. Commun.*, 14, 6218, <https://doi.org/10.1038/s41467-023-41851-0>, 2023.
- Vautard, R., Yiou, P., D’Andrea, F., de Noblet, N., Viovy, N., Casou, C., Polcher, J., Ciais, P., Kageyama, M., and Fan, Y.: Summertime European heat and drought waves induced by wintertime Mediterranean rainfall deficit, *Geophys. Res. Lett.*, 34, <https://doi.org/10.1029/2006GL028001>, 2007.
- Vernay, M., Lafaysse, M., Monteiro, D., Hagenmuller, P., Nheili, R., Samacoïts, R., Verfaillie, D., and Morin, S.: The S2M meteorological and snow cover reanalysis over the French mountainous areas: description and evaluation (1958–2021), *Earth Syst. Sci. Data*, 14, 1707–1733, <https://doi.org/10.5194/essd-14-1707-2022>, 2022.
- Vernay, M., Lafaysse, M., and Hagenmuller, P.: The S2M meteorological and snow cover reanalysis in the French mountainous areas (1958–present), AERIS [data set], <https://doi.org/10.25326/37#v2020.2>, 2023.
- Vidal, J.-P., Martin, E., Franchistéguy, L., Habets, F., Soubeyroux, J.-M., Blanchard, M., and Baillon, M.: Multilevel and multiscale drought reanalysis over France with the Safran-Isba-Modcou hydrometeorological suite, *Hydrol. Earth Syst. Sci.*, 14, 459–478, <https://doi.org/10.5194/hess-14-459-2010>, 2010.
- Walker, A. P., Carter, K. R., Gu, L., Hanson, P. J., Malhotra, A., Norby, R. J., Sebestyen, S. D., Wullschleger, S. D., and Weston, D. J.: Biophysical drivers of seasonal variability in *Sphagnum* gross primary production in a northern temperate bog, *J. Geophys. Res.-Biogeo.*, 122, 1078–1097, <https://doi.org/10.1002/2016JG003711>, 2017.
- Wania, R., Ross, I., and Prentice, I. C.: Integrating peatlands and permafrost into a dynamic global vegetation model: 2. Evaluation and sensitivity of vegetation and carbon cycle processes, *Glob. Biogeochem. Cycles*, 23, <https://doi.org/10.1029/2008GB003413>, 2009.
- Wania, R., Melton, J. R., Hodson, E. L., Poulter, B., Ringeval, B., Spahni, R., Bohn, T., Avis, C. A., Chen, G., Eliseev, A. V., Hopcroft, P. O., Riley, W. J., Subin, Z. M., Tian, H., van Bodegom, P. M., Kleinen, T., Yu, Z. C., Singarayer, J. S., Zürcher, S., Lettenmaier, D. P., Beerling, D. J., Denisov, S. N., Prigent, C., Papa, F., and Kaplan, J. O.: Present state of global wetland extent and wetland methane modelling: methodology of a model inter-comparison project (WETCHIMP), *Geosci. Model Dev.*, 6, 617–641, <https://doi.org/10.5194/gmd-6-617-2013>, 2013.
- Weston, D. J., Timm, C. M., Walker, A. P., Gu, L., Muchero, W., Schmutz, J., Shaw, A. J., Tuskan, G. A., Warren, J. M., and Wullschleger, S. D.: *Sphagnum* physiology in the context of changing climate: emergent influences of genomics, modelling and host–microbiome interactions on understanding ecosystem function, *Plant Cell Environ.*, 38, 1737–1751, <https://doi.org/10.1111/pce.12458>, 2015.
- Williams, T. G. and Flanagan, L. B.: Measuring and modelling environmental influences on photosynthetic gas exchange in *Sphagnum* and *Pleurozium*, *Plant Cell Environ.*, 21, 555–564, <https://doi.org/10.1046/j.1365-3040.1998.00292.x>, 1998.
- World Meteorological Organization: WMO Guidelines on the Calculation of Climate Normals, Wmo-no. 1203, World Meteorological Organization, Geneva, Switzerland, <https://library.wmo.int> (last access: 11 May 2026), 2017.
- Wu, Y. and Blodau, C.: PEATBOG: a biogeochemical model for analyzing coupled carbon and nitrogen dynamics in northern peatlands, *Geosci. Model Dev.*, 6, 1173–1207, <https://doi.org/10.5194/gmd-6-1173-2013>, 2013.

- Wu, Y., Verseghy, D. L., and Melton, J. R.: Integrating peatlands into the coupled Canadian Land Surface Scheme (CLASS) v3.6 and the Canadian Terrestrial Ecosystem Model (CTEM) v2.0, *Geosci. Model Dev.*, 9, 2639–2663, <https://doi.org/10.5194/gmd-9-2639-2016>, 2016.
- Young, D. M., Baird, A. J., Gallego-Sala, A. V., and Loisel, J.: A cautionary tale about using the apparent carbon accumulation rate (aCAR) obtained from peat cores, *Sci. Rep.*, 11, 9547, <https://doi.org/10.1038/s41598-021-88766-8>, 2021.
- Yu, Z.: Holocene carbon flux histories of the world's peatlands: Global carbon-cycle implications, *The Holocene*, 21, 761–774, <https://doi.org/10.1177/0959683610386982>, 2011.
- Yurova, A., Wolf, A., Sagerfors, J., and Nilsson, M.: Variations in net ecosystem exchange of carbon dioxide in a boreal mire: Modeling mechanisms linked to water table position, *J. Geophys. Res.-Biogeo.*, 112, <https://doi.org/10.1029/2006JG000342>, 2007.